Reactive transport modeling of a multiple partially penetrating well (MPPW) system in a heterogeneous, brackish aquifer:

Implications for coastal aquifer storage and recovery (ASR)

PAXTON C. ALBERT: 5852838

UTRECHT UNIVERSITY, FACULTY OF GEOSCIENCES

DEPARTMENT OF EARTH SCIENCES: EARTH SURFACE AND WATER

KWR WATERCYCLE RESEARCH INSTITUTE

KWR

Universiteit Utrecht

Title page photo Credit: Zuurbier, 2016: From Chapter 3 cover page

Statement of originality of the MSc thesis

I declare that:

1. this is an original report, which is entirely my own work,

2. where I have made use of the ideas of other writers, I have acknowledged the

source in all instances,

3. where I have used any diagram or visuals I have acknowledged the source in

all instances,

4. this report has not and will not be submitted elsewhere for academic

assessment in any other academic course.

Student data:

Name: Paxton Albert

Registration number:

5852838

Date: 24/08/2018

Signature: Paxton Albert

Acknowledgments

I would like to thank my advisors Ruud Schotting, Niels Hartog, Koen Zuurbier, and Boris van Breukelen for all of their help and support in completing this endeavor. I have learned so much from you all and will take these lessons with me wherever I go. I would also like to thank KWR Watercycle Research Institute for allowing me to work on a world-class project with them and for allowing me to use their lovely office space.

I want to thank my parents, younger brother, and Loes for all of the emotional support that you all provided me throughout this stressful project. Without you, I would not be who I am today and I am forever grateful for the love and support you have all shown me throughout the years.

Table of Contents

Acknowledgments iv

List of Figures vii

Abstract 0

1. Introduction 0

2. Methods and Materials 2

2.1 The Study Area 2

2.1.1 Aquifer Characterization 3

2.1.1.1 Hydrogeological Units 3

2.1.1.2 Geochemical Units and Characterization 3

2.1.2 MPPW-ASR Setup 5

2.2 The Data Sets 7

2.3 Selection of Processes 7

2.3.1 Determining the Extent of Pyrite Oxidation 7

2.3.2 Kinetic Pyrite (FeS_2) Oxidation 7

2.3.3 Kinetic Fe-Mn-Carbonate Dissolution 9

2.4 The Model Input 9

2.4.1 Axisymmetric Setup and Model Framework 9

2.4.2 SEAWAT Model 10

2.4.3 PHT3D Model 12

3.4.4 Model Assumptions 12

3. Results 13

3.1 Geochemical Analysis 13

3.1.1 Observed Trends for Na^+ 13

3.1.2 Observed Trends for Fe^{2+} and Mn^{2+} 14

3.1.3 Mobilization of Fe^{2+} and Mn^{2+} 15

3.1.4 Equilibrium Calcite Dissolution 17

3.1.5 Conservative SO_4^{2-} 18

3.1.6 Analysis of Pyrite Oxidation 19

3.1.6.1 Extent of pyrite oxidation 19

3.1.6.2 PHREEQC modeling of pyrite oxidation 19

3.1.7 Observed Trends for As and Zn^{2+} 20

3.1.8 Trace Metal Mobilization 20

3.2 Modeling of Dominant Processes 23
3.2.1 Flow Validation 23
3.2.2 Cation-Exchange and Equilibrium Calcite Dissolution 24
3.2.2.1 Simulation of observed trends in Na^+ 24
3.2.2.2 Effects of decommissioning the well for Na^+ 24
3.2.2.3 Assessment of equilibrium cation-exchange and calcite dissolution on Ca^{2+} 24
3.2.2.4 Effects of cation-exchange on Fe^{2+} and Mn^{2+} 24
3.2.3 Kinetic Pyrite Oxidation 26
3.2.3.1 Reproduction of Ca^{2+} concentrations observed at Nootdorp 26
3.2.3.2 Pyrite oxidation effects on SO_4^{2-} and Fe^{2+} concentrations 26
3.2.4 Fe-Mn-Minerals at Nootdorp 27
3.2.4.1 Equilibrium modeling with Fe^{2+}, Mn^{2+}, $Fe(OH)_3$, and MnO_2 27
3.2.4.2 Kinetic dissolution of Fe-Mn-carbonates and reproduction of trends for Fe^{2+} and Mn^{2+} 28
3.2.4.3 Injection water impacts on Fe^{2+} and Mn^{2+} 28
3.2.4.4 Decommissioning effects on $Fe^{2+}$and Mn^{2+} 28
4. Discussion 30
4.1 MPPW-ASR and Reactive Impacts on the Injected Freshwater 30
4.1.1 Dominance of Cation-Exchange in a Coastal Aquifer 30
4.1.2 Redox Processes in a Coastal Aquifer 30
4.1.2.1 MPPW-ASR and ongoing pyrite oxidation 30
4.1.2.2 Mobilization and oxidation of Fe^{2+} and Mn^{2+} 31
4.1.3 Overall Assessment of the Impact of MPPW-ASR on the Injection Water 32
4.2 MPPW-ASR Reactive Impact on Surrounding Brackish Water 33
4.3 Model Limitations and Potential Modeling 33
4.3.1 Limitations and Remarks for Modeling Nootdorp 33
4.3.2 Further Modeling 34
5. Conclusion 34
6. References 35

List of Figures

Figure 1: Schematic drawing of what a typical ASR system looks like upon injection of newly sourced freshwater into ambient brackish water of the chosen aquifer. The resulting stored water acts as a so called “bubble” upon injection, and displaces the heavier, ambient water. [Zuurbier et al, 2017]. 1
Figure 2: A map that shows the location of the Nootdorp ASR site along with the regional head contours [TNO, 1995] and the varying chloride concentrations [Oude Essink et al., 2010]. The black triangle indicates the location of the Nootdorp site [Zuurbier,2016]..... 3
Figure 3: A schematic demonstrating the distribution between hydrogeological and geochemical units at the Nootdorp aquifer. This is also coupled with the ASR-well locations for better visualization of the subsurface. HU-e and GU-III are areas of great interest due to its high reactivity coupled with its complex hydrogeological properties [Zuurbier et al., 2016]..... 4
Figure 4: The Nootdorp ASR-site and the multiple partially penetrating well system configuration visualized [Zuurbier, 2014]. Injection (mainly at AWS3-AWS4) and abstraction (mainly at AWS1-AWS2) of freshwater occurs near the Northwestern area of the greenhouse. Three sets of monitoring wells towards the Southeast were equipped at the site to collect hydrological and geochemical data. The water abstracted at Nootdorp is used for irrigation of the greenhouse located near the ASR-system..... 6
Figure 5: Schematic figure of the axial-symmetric setup for the Nootdorp model. The first 100 m are discretized into cells that are 1m in length. The remaining 2900 m are discretized into 10 m intervals. Constant head boundaries were placed in all cells along the row at -4m BSL, -80m BSL (at the base of aquifer 2), and along the last column 3000 m away from the ASR-wells..... 10
Figure 6: A detailed graph showing the volumes of water that have been infiltrated and recovered at Nootdorp. The data from this graph is the pumping data that was used in order to simulate the density-dependent flow at Nootdorp and help validate the model..... 11
Figure 7: Cl vs. Na concentrations during the first cycle (a) and the fifth and sixth cycle (b). (a) Represents the higher concentrations seen in the beginning of the ASR operation while (b) demonstrates the decrease in concentrations for both species after 5 years of operation..... 14
Figure 8: (a) Iron versus Manganese concentrations observed at the ASR-wells and (b) at the first monitoring well 5m away. Compared to previous cycles, Cycles 5 and 6 are met with higher Mn:Fe ratios, but lower concentrations for both species overall. A 1:2 ratio line was added in order to represent ongoing MnO_2 reduction. 16
Figure 9: Ca^{2+} concentrations vs. HCO_3^- concentrations observed for all Cycles of the ASR-pilot. The observed concentrations for Ca are higher than predicted values for equilibrium calcite dissolution. Injection of Ca also does not explain the concentrations indicating other processes are producing the higher concentrations..... 17
Figure 10: SO4 vs. Cl concentrations. In order to assess whether SO4 is conservative, lines of expected values for SO4:Cl ratios were plotted with the observed data points. One point at AWS4 shows much higher SO4:Cl ratio than other observed points. This point was seen with a negative BEX and after an increase in NO_3, which potentially caused the high SO_4 value through oxidation of pyrite by nitrate..... 18
Figure 11: Evolution of Arsenic (Top) and Zinc (bottom) concentrations at the ASR-wells, listed by Cycle. Increases in both trace metals were observed in Cycle 1, but overall have decreased after multiple ASR cycles..... 21
Figure 12: Arsenic vs. sulfate (left) and zinc vs. sulfate (right). The observed As concentrations are lower than expected when looking at the ratio line for As:SO4 release from pyrite. The right graph demonstrates many points falling along the ratio line for Zn:SO4 release from the bottom of the well.. 22

Figure 13: Observed Chloride concentrations plotted with simulated Chloride concentrations at AWS1 and AWS2. Observed results plot along the simulated results, but simulated results tend to be slightly higher than the observed concentrations. 23
Figure 14: Simulated calcium(black) and sodium(red) concentrations for scenarios 1-4 (listed in section 2.4.3) plotted with observed calcium (blue circles) and sodium (black plusses) concentrations for AWS1 (top) and AWS2 (bottom). 25
Figure 15: Observed SO_4^{2-} concentrations plotted with modeled SO_4^{2-} concentrations in order to compare how the model results match up with the observed points. Depending on the location of the well, the model output was either higher or lower than observed SO_4^{2-} concentrations. This likely has to do with the vertically heterogeneous nature of the aquifer, where dominant mineral interactions vary. 27
Figure 16: (a) The $Fe^{2+}$and Mn^{2+}concentrations at AWS1 and (b) the $Fe^{2+}$and Mn^{2+}concentrations at AWS2 for the different scenarios 1-4, listed in section 2.4.3, plotted with the observed concentrations for Fe^{2+} (red dots) and Mn^{2+} (black pluses). The figures for $Fe^{2+}$and Mn^{2} in (a) were split up in order to see the dynamic changes occurring in the initial cycles of ASR. 29

Abstract

The reactive transport impacts of a multiple partially-penetrating well (MPPW-)ASR system in a brackish, heterogeneous coastal aquifer are complex due to geochemical heterogeneities, cation-exchange, mineral dissolution, and redox processes, as well as complex fluid flow induced by density-differences between the injection water and ambient water. To understand the impact of relevant processes during MPPW-ASR, a reactive transport model was setup based on geochemical observations to evaluate the long-term impacts on the injected freshwater and the surrounding brackish water, which is diluted partially by the freshwater. It was found that the major impacts on the injection water during the initial cycles of MPPW-ASR were cation-exchange, Fe-Mn-carbonate dissolution, pyrite oxidation, and MnO_2 reduction by Fe^{2+}, whereas in later cycles the water composition was impacted by pyrite oxidation, trace metal sorption, oxidation of Fe^{2+} and Mn^{2+}, and the reduction of MnO_2 by Fe^{2+}. The surrounding brackish water is diluted by the injected freshwater and forms a water type which is depleted in Na^+ and enriched in HCO_3^- in the initial cycles but becomes enriched in Na^+ and Cl^- in later cycles. This water type is then transported away from the ASR-well, as well as towards the shallower intervals of the aquifer, maintaining its composition. The results of this project indicate that redox processes still affect the composition of the injected freshwater and the surrounding brackish water around the freshwater bubble is an undesirable water-type that could potentially harm the quality of the injection water.

1. Introduction

Aquifer storage and recovery (ASR) is an important technique used for freshwater sustainability in areas where shortage of water can occur. It involves injecting surplus water (i.e. rainwater, urban-wastewater, etc.) into an aquifer for storage and recovery of the stored water for later use [Pyne, 2005; Ward et al., 2009; Zuurbier et al., 2016]. Using ASR can help balance the water supply with demand in many areas of the world in a cost-effective manner [Pyne, 2005; Antoniou et al., 2015]. In coastal areas, freshwater demand is typically high, while freshwater supply is low [Ros and Zuurbier, 2017]. Using ASR in coastal aquifers can therefore be applied in order to increase the supply of freshwater for the surrounding area.

Unfortunately, with climate-change and increasing sea-level rise occurring, freshwater aquifers in coastal areas of the world are threatened by an increased rate of salinization [Oude Essink, et al., 2010]. The salinization of these aquifers will subsequently deteriorate the quality of water that could potentially be used for drinking, irrigation, and other applications. Density-effects induced by the injection of freshwater into heavier, brackish water located in coastal aquifers affect the transport of the injected freshwater [Missimer et al., 2002; Ward et al., 2007, 2009]. Low-density freshwater displaces the higher-density ambient water and forms a so called “bubble” at the injection well (Figure 1) [Lowry and Anderson, 2006].

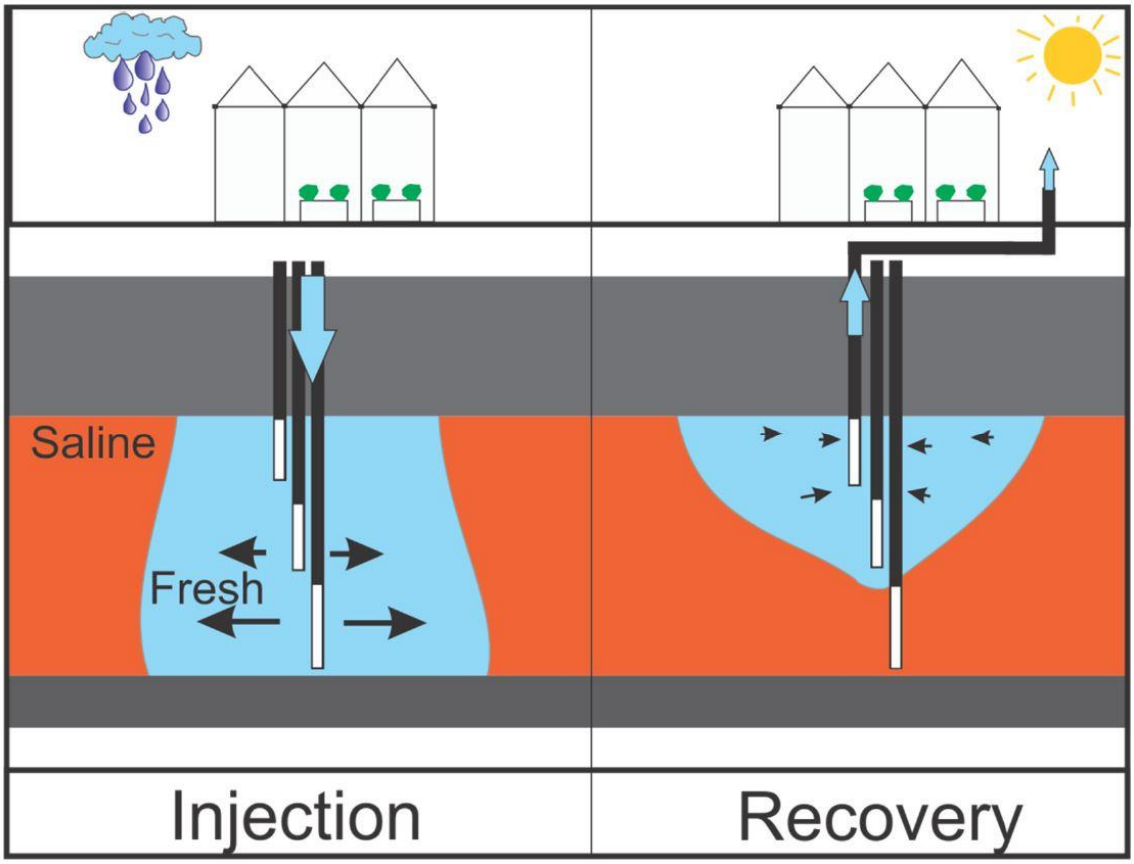

Figure 1: Schematic drawing of what a typical ASR system looks like upon injection of newly sourced freshwater into ambient brackish water of the chosen aquifer. The resulting stored water acts as a so called "bubble" upon injection, and displaces the heavier, ambient water. [Zuurbier et al, 2017].

While the threat of salinization of a well is of concern during ASR, geochemical processes caused by injection of a dissimilar water-type is also an issue [Herczeg et al., 2004, Izbicki et al., 2010]. As water from another source is injected into an aquifer, the injected water will mix with the surrounding water at the fringe where these two waters meet and with the aquifer matrix. Depending on the composition of both water-types and the aquifer mineral matrix, different geochemical processes can occur. This will potentially lead to a positive, negative, or neutral effect on the quality of water, depending on the standards that are set for the ASR-well. Understanding the complex combination of these processes that occur in coastal sites is important due to the large impact it has on the success of ASR.

Recently, Zuurbier et al., 2016 demonstrated the viability of using a multiple partially-penetrating well aquifer storage and recovery (MPPW-ASR) system to increase the recovery efficiency (RE) of injected freshwater in a brackish, coastal aquifer. The RE is the amount of water that can be recovered from the aquifer with a certain standard of quality, with respect to how much water was injected. In Zuurbier et al., 2016, a pilot was set up in Nootdorp, The Netherlands where a coastal aquifer was equipped with a MPPW-ASR system. The water taken from this coastal aquifer was to be used for irrigation and the standards for the quality of water were strict regarding Na^{+}, Fe^{2+}, and Mn^{2+}. Zuurbier et al., 2016 described in detail the results of a geochemical analysis done on the ambient water and aquifer, as well

as created a reactive-transport model that could simulate equilibrium cation-exchange. This resulted in a model that could accurately simulate Na^+ trends observed at Nootdorp.

While equilibrium cation-exchange and calcite dissolution were included in the model of Zuurbier et al., 2016, important redox processes, such as pyrite oxidation, were not included. These complex processes have a direct influence on the recovered water quality at Nootdorp, as they often release or retard undesirable constituents, such as Fe^{2+} and Mn^{2+}, in the oxygen-rich injected freshwater. By creating a model that integrates equilibrium cation-exchange with the more complicated redox/mineral processes that threaten the RE at Nootdorp, long-term assessments of the impact MPPW-ASR has on coastal aquifers can be done.

Therefore, in this study, new geochemical data taken from the Nootdorp MPPW-ASR pilot in 2015-2017 was used to assess what geochemical processes are dominant during MPPW-ASR. With this analysis, the aim of this project was to create a more complete reactive-transport model that can further describe the geochemical and physical processes that are occurring at the site. By reproducing important trends observed at Nootdorp, the overall impact that MPPW-ASR has on coastal aquifers could be evaluated. This resulted in reactive-transport model that can be used to simulate a myriad of processes and chemical species during MPPW-ASR to help further understand the impact that it has on coastal aquifers long-term, as well as its impact on the surrounding groundwater.

2. Methods and Materials

2.1 The Study Area

The focused-on site is an ASR-pilot that was set-up in Nootdorp, The Netherlands (Figure 2). Nootdorp is located between the cities of Rotterdam and The Hague in the province of Zuid Holland and is ~12 km inland from the Dutch North Sea. The site is in an area that is predominantly used for horticulture, and groundwater usage is mainly for irrigation. The Nootdorp field site is a small-scale ASR pilot built in 2011 to store surplus rainwater from the roofs of a 20,000 m^2 greenhouse into an aquifer for times of water shortage. The ASR-pilot is located in a deep polder where brackish seepage to the surface waters occurs [Zuurbier et al., 2014], but the lateral background flow is considered negligible. Its geology is composed of Pleistocene and Holocene fluvial sediments, which can be viewed in the upper ~120 meters [Zuurbier et al., 2016].

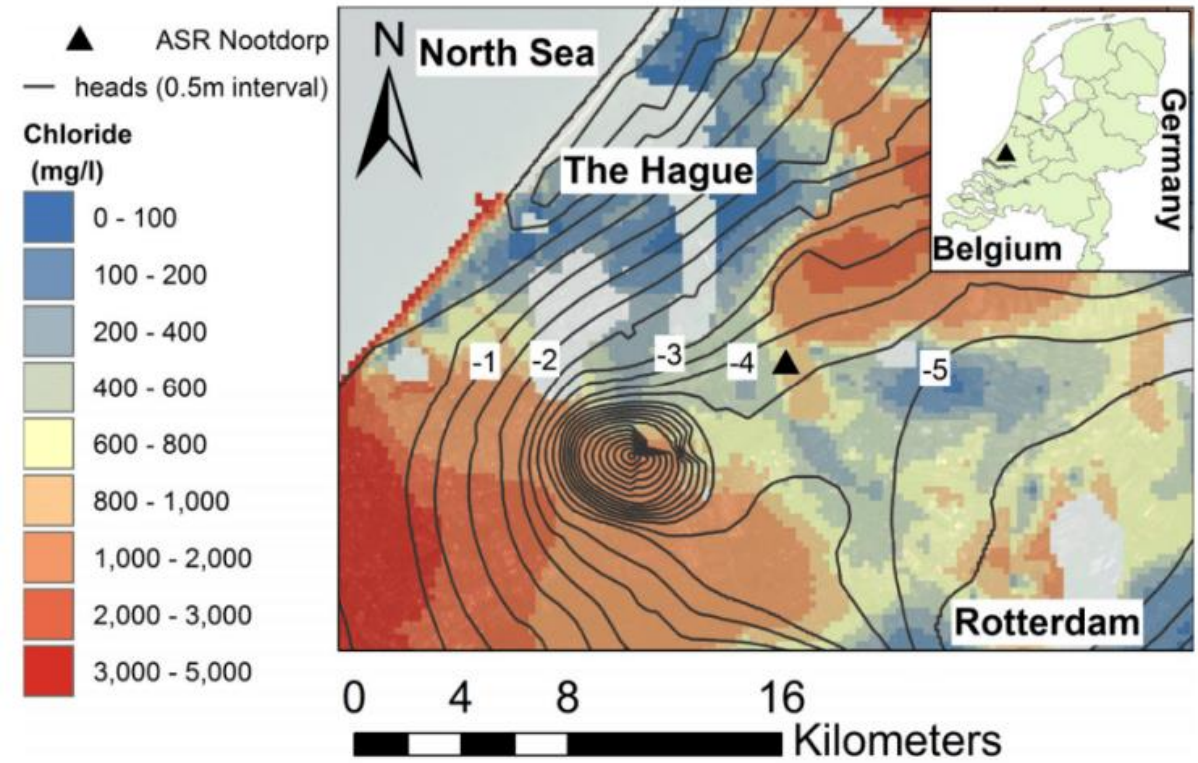

Figure 2: A map that shows the location of the Nootdorp ASR site along with the regional head contours [TNO, 1995] and the varying chloride concentrations [Oude Essink et al., 2010]. The black triangle indicates the location of the Nootdorp site [Zuurbier,2016]

2.1.1 Aquifer Characterization

2.1.1.1 Hydrogeological Units

At the Noordorp site, the target aquifer (~13 – 41m BSL) has been split up into 9 separate units (HU-a to HU-i) based on the hydraulic characteristics observed (Figure 3). Each unit has varying values for their hydraulic conductivity, porosity, grain size (Table 1). The target aquifer is confined between 2 clay and peat intervals and is underlain by a second aquifer (~55-80m BSL). The target aquifer is made up of mostly middle course sands at the top (HU-a to HU-d; ~13 – 28m BSL) while the bottom of the aquifer (HU-f to HU-I; ~31-41m BSL) consists of fine to gravelly very course sands. In HU-e (~28-31m BSL), thin layers of clay, reworked peat, and clay pebbles were found within a matrix consisting of mostly middle course sands. This clay layer is considered non-continuous.

2.1.1.2 Geochemical Units and Characterization

With the site split up into different units based on the hydrogeological properties observed, the site was further characterized into five different units (GU-I to GU-V) based on geochemical observations (Figure 3). The shallower geochemical units (GU-I to GU-II) are characteristic of having a high carbonate content and low pyrite and sedimentary organic matter (SOM) content. The bottom units (GU-IV and GU-V) contain small amounts of carbonate and SOM, but a higher pyrite content. It was also deduced that Fe-Mn-bearing carbonates were present in GU-IV and GU-V. The most reactive unit, GU-III, is indicative of a high SOM, Pyrite, and carbonate content, as well as having a large cation exchange capacity (CEC). Table

2 is a list of geochemical properties and their values based on each geochemical unit. For more information as to how these values were obtained, the reader is referred to Zuurbier et al., 2016.

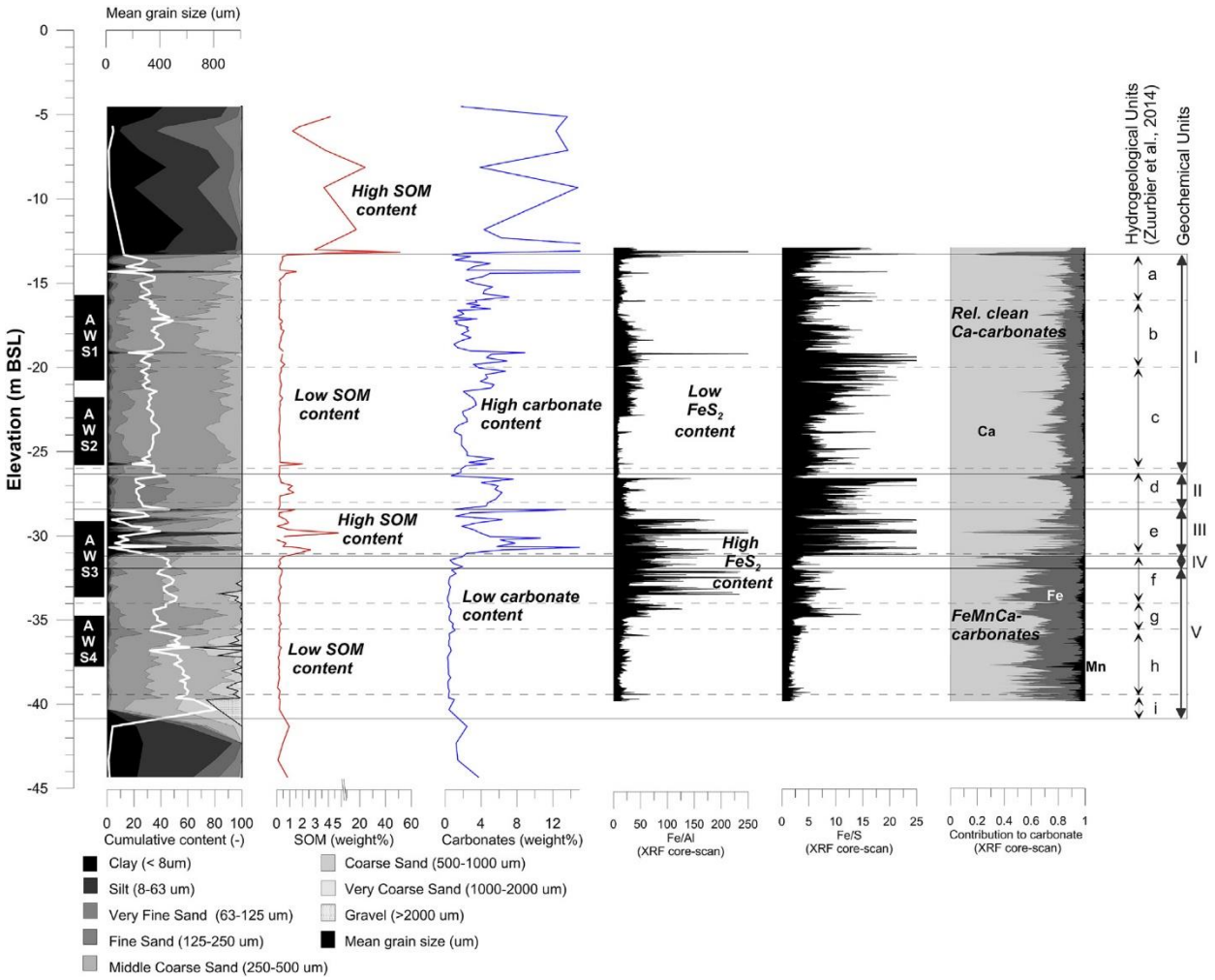

Figure 3: A schematic demonstrating the distribution between hydrogeological and geochemical units at the Nootdorp aquifer. This is also coupled with the ASR-well locations for better visualization of the subsurface. HU-e and GU-III are areas of great interest due to its high reactivity coupled with its complex hydrogeological properties [Zuurbier et al., 2016].

Hydrogeological Unit	**Hydraulic Conductivity (m/d)**	**Specific Storage (m^{-1})**	**Longitudinal Dispersivity (m)**
A	35	1E-7	0.3
B	45	1E-7	0.3
C	35	1E-7	0.5
D	20	1E-7	0.5
E	25	1E-5	0.2
F	80	1E-8	0.2
G	45	1E-8	0.1
H	150	1E-8	0.1
I	400	1E-8	0.1

Table 1: Table that lists some physical parameters and their respected values for the different hydrogeological units that were defined at the Nootdorp site. Values were taken from Zuurbier et al., 2014.

Parameter (Units)	GU-I	GU-II	GU-III	GU-IV	GU-V
Depth (m BSL)	13.16 – 26.57	26.57 – 28.42	28.42 – 31.12	31.12 – 31.82	31.82 – 41.32
Clay Fraction (% d.w.)	0.69	0.77	4.75	0.66	0.51
Gravel Fraction (% d.w.)	0.00	0.00	0.00	0.00	4.15
SOM (% d.w.)	0.41	0.51	1.02	0.27	0.22
Carbonates (% d.w.)	4.38	5.32	4.90	0.82	0.44
Total C (% d.w.)	0.56	0.69	1.25	0.07	0.07
CEC (meq/kg)	12.0	14.3	51.1	7.1	6.0
Pyrite (% d.w.)	0.06	0.09	1.05	0.90	0.28
Fe_2O_3 (% d.w.)	0.55	0.71	1.72	0.86	0.40
Fe-reactive, non-pyrite (%d.w.)	0.10	0.24	0.42	0.05	0.02
MnO (% d.w.)	0.01	0.02	0.03	0.01	< 0.01

Table 2: A table that contains basic information about the geochemical content that makes up the Nootdorp ASR site. Geochemical values were obtained in Zuurbier et al., 2016.

2.1.2 MPPW-ASR Setup

The ASR-pilot was equipped with a MPPW-ASR system to test the feasibility of increasing the RE through this well configuration (Figure 4). In table 3, the depths and distance at which each well screen is located are listed. The four ASR-wells (AWS1-AWS4) were used for injecting the freshwater into the aquifer during the beginning of the pilot. After the first three months of the operation, AWS1 was mainly used for recovery, the bottom 2 wells were mainly used for injection, and AWS2 varied between recovery and injecting. 5m away from the ASR-wells are the first set of monitoring wells (MW1S0-MW1S5). There are 6 of these wells at varying depths, which were used to take geochemical and hydrogeological measurements during the ASR-pilot. At 15m away from the ASR-wells are five more monitoring wells at varying depths (MW2S0-MW2S4) (Table 3).

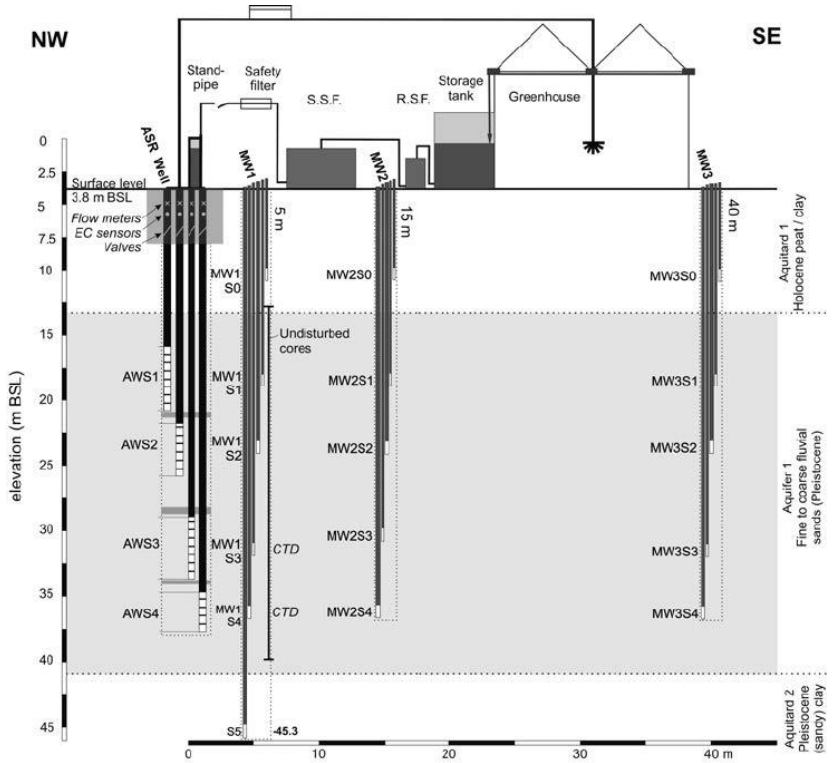

Figure 4: The Nootdorp ASR-site and the multiple partially penetrating well system configuration visualized [Zuurbier et al., 2014]. Injection (mainly at AWS3-AWS4) and abstraction (mainly at AWS1-AWS2) of freshwater occurs near the Northwestern area of the greenhouse. Three sets of monitoring wells towards the Southeast were equipped at the site to collect hydrological and geochemical data. The water abstracted at Nootdorp is used for irrigation of the greenhouse located near the ASR-system.

Well Screen	Well Screen Top (m BSL)	Well Screen Bottom (m BSL)
AWS1	-15.8	-20.8
AWS2	-21.8	-25.8
AWS3	-29.2	-33.7
AWS4	-34.7	-37.7
MW1S0	-9.82	-10.82
MW1S1	-17.97	-18.97
MW1S2	-23.12	-24.12
MW1S3	-30.92	-31.92
MW1S4	-35.72	-36.72
MW1S5	-44.82	-45.82
MW2S0	-9.77	-10.77
MW2S1	-17.77	-18.77
MW2S2	-23.22	-24.22
MW2S3	-29.77	-30.77
MW2S4	-35.62	-36.62

Table 3: List of the depths for each well screen at the Nootdorp ASR site. The first set of monitoring wells (MW1S0-MW1S5) are located 5 meters Southeast of the ASR-wells, and the second set of monitoring wells (MW2S0-MW2S4) are located 15 meters Southeast of the ASR-wells.

2.2 The Data Sets

For this study, 2 different sets of chemical data were provided by KWR Watercycle Research Institute in Nieuwegein, the Netherlands. The first set of chemical data was taken at least monthly in 2011-2013 from the ASR-wells and monitoring wells. During this time, water samples were collected and sent to VU University Water Lab analysis lab to determine each sample's chemical makeup. For more information relating to the processes that took place to obtain the geochemical data, the reader is referred to Zuurbier et al., 2016.

The second set of chemical data was taken during the ASR-pilot in 2015-2017. The samples taken during this time were collected bi-monthly from the ASR and monitoring wells and samples were sent to the WUR University Water Lab. This second data set differed from the first due to the fact that each of the 2 labs evaluated the water chemistry with different detection limits for certain chemical species (mainly Fe^{2+}, Mn^{2+}, Zn^{2+}, and As). Along with the chemical data, an EXCEL document containing the pumping data taken from flowmeters at the ASR-site was also provided.

2.3 Selection of Processes

To assess the processes that were potentially occurring in the target aquifer, a geochemical analysis was performed using the chemical data sets provided. Using stoichiometric ratios based on relevant reactions (Table 4), several plots of the data sets were made. This was done to determine the dominant processes occurring in the aquifer over time for the model. Processes that had a profound effect on the water quality based on the geochemical analysis were added to the reaction network of the model. As cation-exchange was already deemed important in Zuurbier et al., 2016 to describe the fate of Na^+, it was automatically included into the reaction network. In table 4, the reaction network and relevant reactions that were used in this study based on geochemical observations are listed. These specific reactions were considered to be the most prevalent reactions that threatened the quality of water at the Nootdorp site.

2.3.1 Determining the Extent of Pyrite Oxidation

To measure the amount of oxygen that is consumed due to pyrite oxidation, the below equation from Zuurbier et al., 2016 was used:

$$\Delta C(O_{2(pyrite)}) = \frac{3.75}{2}\left[C(SO_4) - C\left(SO_{4(injection)}\right) - C\left(SO_{4(nitrate)}\right)\right] \quad (1)$$

where $\Delta C(O_{2(pyrite)})$ is the amount of oxygen consumed due to pyrite oxidation, $C(SO_4)$ is the molar concentration of SO_4^{2-} measured upon injection, $C(SO_{4(injection)})$is the molar concentration of SO_4^{2-} that is measured in the injection water, and $C(SO_{4(nitrate)})$ is determined by the following equation:

$$C\left(SO_{4(nitrate)}\right) = \frac{10}{14}\left[C\left(NO_{3(injection)}\right) - C(NO_3)\right] \quad (2)$$

where $C\left(NO_{3(injection)}\right)$ is the molar concentration of NO_3^- that was measured in the injection water and $C(NO_3)$is the molar concentration of NO_3^- measured in the aquifer during storage.

2.3.2 Kinetic Pyrite (FeS_2) Oxidation

The simulation of kinetic pyrite oxidation was required during this study. The general form for kinetic mineral dissolution was used:

$$R_{pyr} = k_{pyr}\frac{A_{pyr}}{V}\left(\frac{m}{m_0}\right)^n_{pyr} g(C) \quad (3)$$

where R_{pyr} is the overall rate of the reaction [mol/L/s], k_{pyr} is the specific rate constant for the reaction [mol/dm^2/s], which has a value of $10^{-10.19}$ for the oxidation of pyrite by dissolved oxygen [Williamson and Rimstidt, 1994], A_{pyr} is the initial surface area of pyrite [dm^2], V is the volume of the solution [dm^3], $(m/m_0)^n$ is a factor that takes into account the changes in reactive surface sites as the reaction progresses [Appelo and Postma, 2005], and $g(C)$ is a function that takes into account the solution composition effects on the rate. For kinetic pyrite oxidation, the function that was used to describe this process is from Williamson and Rimstidt, 1994:

$$g(C) = \frac{m_{DO}^{0.5(\pm 0.04)}}{m_{H+}^{0.11(\pm 0.01)}} \qquad (4)$$

Where m_{DO} is the concentration of dissolved oxygen in solution [mol/L] and m_{H+} is the concentration of protons in solution [mol/L]. The initial surface area was calculated assuming a grain size of 1mm, a porosity of 0.3 [-], and a bulk density of 2650 kg/m^3. The value n was assumed to be 2/3, which is used to describe a monodisperse population of uniform growing or dissolving spheres and cubes [Appelo and Postma, 2005].

Included in Model	Cation-Exchange	
X	**Freshening**	$aCa^{2+} + [bNa, cMg, dK, eNH_4, fFe, gMn] - X \rightarrow bNa^{+} + cMg^{2+} + dK^{+} + eNH_4 + fFe^{2+} + gMn^{2+} + [aCa] - X$
X	**Salinization**	$bNa^{+} + cMg^{2+} + dK^{+} + eNH_4 + fFe^{2+} + gMn^{2+} + [aCa] - X \rightarrow aCa^{2+} + [bNa, cMg, dK, eNH_4, fFe, gMn] - X$
	Equilibrium Dissolution	
X	**Calcite dissolution (upon proton buffering)**	$2H^{+} + CaCO_3 \rightarrow Ca^{2+} + CO_2 + H_2O$
X	**Calcite dissolution (upon CO_2 production)**	$CO_2 + CaCO_3 + H_2O \rightarrow Ca^{2+} + 2HCO_3^{-}$
	Redox Processes	
X	**Pyrite-oxidation by O_2**	$3.75O_2 + FeS_2 + 3.5H_2O \rightarrow Fe(OH)_3 + 2SO_4^{2-} + 4H^{+}$
	Pyrite-oxidation by NO_3^-	$14NO_3 + 5FeS_2 + 4H^{+} \rightarrow 5Fe^{2+} + 10SO_4^{2-} + 7N_2 + 2H_2O$
	Oxidation of organic matter by O_2	$O_2 + CH_2O \rightarrow CO_2 + H_2O$
	Oxidation of organic matter by NO_3^-	$NO_3^{-} + 1.25CH_2O \rightarrow 0.5N_2 + HCO_3^{-} + 0.75H_2O + 0.25CO_2$
X	**Fe-carbonate oxidation**	$0.25O_2 + FeCO_3 \rightarrow Fe(OH)_3 + CO_2$
X	**Mn-carbonate oxidation**	$0.5O_2 + MnCO_3 \rightarrow MnO_2 + CO_2$
X	**Fe^{2+} oxidation (dissolved)**	$Fe^{2+} + 0.25O_2 + 2.5H_2O \rightarrow Fe(OH)_3 + 2H^{+}$
X	**Mn^{2+} oxidation (dissolved)**	$Mn^{2+} + 0.5O_2 + H_2O \rightarrow MnO_2 + 2H^{+}$
	Fe^{2+} oxidation (adsorbed)	$Fe - X_2 + 0.25O_2 + CaCO_3 + 1.5H_2O \rightarrow Ca - X_2 + Fe(OH)_3 + CO_2$
	Mn^{2+} oxidation (adsorbed)	$Mn - X_2 + 0.5O_2 + CaCO_3 \rightarrow Ca - X_2 + MnO_2 + CO_2$
X	**MnO_2 reduction by Fe^{2+}**	$MnO_2 + 2Fe^{2+} + 4H_2O \rightarrow 2Fe(OH)_3 + Mn^{2+} + 2H^{+}$
	MnO_2 reduction by DOC	$MnO_2 + 0.5CH_2O + 1.5CO_2 + 0.5H_2O \rightarrow Mn^{2+} + 2HCO_3^{-}$
	$Fe(OH)_3$ reduction by DOC	$Fe(OH)_3 + 0.25CH_2O + 1.75CO_2 \rightarrow Fe^{2+} + 2HCO_3^{-} + 0.75H_2O$
	Nitrification	$4O_2 + 2NH_4^{+} \rightarrow 2NO_3^{-} + 2H_2O + 4H^{+}$

Table 4: Processes that were recognized based on geochemical observations and modeling from Nootdorp. The reaction network that was used for modeling the Nootdorp geochemistry is marked by the X in the left-most column, while the remaining reactions are relevant to explain particular trends.

2.3.3 Kinetic Fe-Mn-Carbonate Dissolution

At the Nootdorp site, the presence of Fe-Mn-carbonates were thought to be the source of the unwanted Fe^{2+} and Mn^{2+} arriving at the recovery wells and threatening the success of the ASR-well [Zuurbier et al, 2016]. To simulate this, rhodochrosite ($MnCO_3$) and siderite ($FeCO_3$) were added to the reaction network of the model. While it is unclear whether the Fe-Mn-carbonates are individual carbonates or a mixed phase, such as Ankerite ((Ca, Fe, Mn, Mg)$(CO_3)_2$), the heterogeneous nature of the aquifer required that both rhodochrosite and siderite be simulated as separate phases. The kinetic rate equation used for dissolution of both minerals was taken from Antoniou et al., 2013 and is listed below:

$$R_{Fe,Mn-carb} = (k_1[H^+]^{0.65} + k_2[CO_2]^{0.65} + k_3)(\frac{A_{Fe,Mn-carb}}{V})(\frac{m}{m_0})^{0.67}_{Fe,Mn-carb}(1 - SR_{Fe,Mn-carb}) \quad (5)$$

where the brackets indicate activities [-], k_1, k_2, k_3 are rate constants with values of 2.6 x 10^{-5}, 10^{-6}, and 2.2 x 10^{-10} [mol/dm^2/s], $A_{Fe,Mn-carb}$ is the initial surface area for rhodochrosite or siderite [dm^2], V is the solution volume [dm^3], and $SR_{Fe,Mn-carb}$ is the saturation ratio specific to rhodochrosite or siderite.

2.4 The Model Input

2.4.1 Axisymmetric Setup and Model Framework

To model the Nootdorp site, the FloPy package for the Python programming language was used. The FloPy package allows users to create, run, and post-process MODFLOW-based models all within a simple Python script. Because there are many scientific packages available for Python, using FloPy in tandem with other packages allows the user to further analyze model results that might otherwise be difficult to do within a graphical user interface (GUI) [Bakker, 2016]. Within FloPy, the model framework was set up in a two-dimensional axial-symmetric configuration (Figure 5). Two-dimensional axial-symmetric modeling required the adjustment to a set of physical parameters to account for the increase in flow area with increasing radial distance from the well. By creating the model in this configuration, run-times for modeling decrease substantially when compared to the run-times if a traditional three-dimensional model were used [Langevin, 2008]. For further explanation as to how axial-symmetric modeling is performed, the reader is referred to Langevin, 2008.

The model extent was set to be 3000 m in the r-direction and 80m in the z-direction. The extended length in the r-direction was added in order to prevent edge effects that are caused by the constant head boundary. It was then discretized into 57 cells in the z-direction and 390 cells in the r-direction. The lengths of the cells in the z-direction in the target aquifer and underlying aquitard were set to 1 m but varied minimally in the overlying aquitard. In the r-direction, the cell lengths were set 1 m for the first 100 cells but were then set to 10 m for the remaining 290 cells.

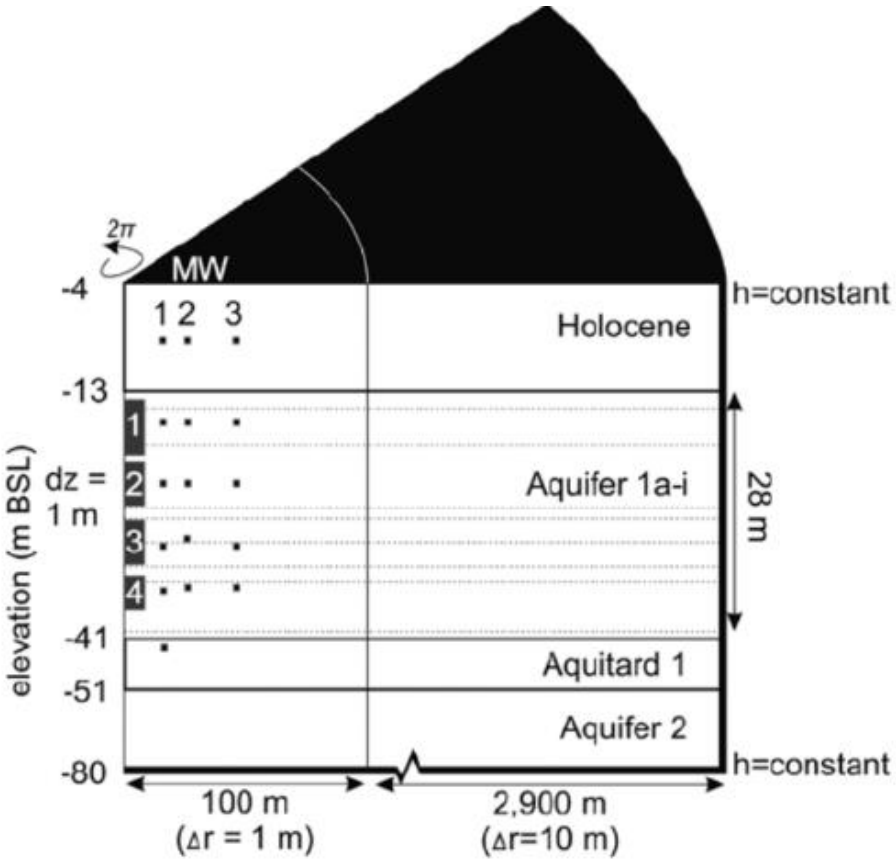

Figure 5: Schematic figure of the axial-symmetric setup for the Nootdorp model. The first 100 m are discretized into cells that are 1m in length. The remaining 2900 m are discretized into 10 m intervals. Constant head boundaries were placed in all cells along the row at -4m BSL, -80m BSL (at the base of aquifer 2), and along the last column 3000 m away from the ASR-wells [Zuurbier et al., 2014].

2.4.2 SEAWAT Model

After the framework of the model was created, the next step taken was to model the groundwater flow. To achieve this, a SEAWAT [Langevin et al., 2007] model was created in FloPy. SEAWAT is a computer program that couples the codes MODFLOW and MT3DMS to simulate three-dimensional variable-density groundwater flow. With SEAWAT, the ability to model groundwater flow and conservative transport of solutes all while taking into account density differences that are present in the aquifer was possible [Langevin, 2008].

Three constant head boundaries were placed within the model domain, as well as three constant sink/source boundaries in the same positions. They were placed at the top of the overlying holocene aquitard with a head of -4.8m BSL, at the base of aquifer 2 with a value of -4.3m BSL, and the final boundary was placed along the final column 3000 m away from the ASR wells. The densities of the ambient water were calculated using the concentration of total dissolved solids (TDS) measured in the field [Zuurbier et al., 2014]. Six field cycles, followed by two fictitious cycles, were included in the model (Table 5). For Cycles 1-6, pumping data from the ASR-pilot was used (Figure 6) and a simplified pumping and injection scheme was used for the two fictitious cycles to accentuate the processes occurring during freshening and salinization. Daily stress periods were used in order to accurately model the complex processes that were occurring.

Table 5: The ASR-phases that have occurred at Nootdorp and the simulated subsequent cycles that were used in order to model the flow. Due to the complex injection scheme that the MPPW-ASR site underwent, a graph showing the infiltration, net infiltration, and recovered volumes will be presented below.

Phase	Year	Length (days)	Pumping Scheme
Cycle 1	2012	273	Flowmeters
Cycle 2	2013	338	Flowmeters
Cycle 3	2014	335	Flowmeters
Cycle 4	2015	456	Flowmeters
Cycle 5	2016	328	Flowmeters
Cycle 6	2017	294	Flowmeters
Injection Cycle 7	2018	150	Q_{tot} = 133.3 m^3/day
Idle Cycle 7	2018	30	None
Pumping Cycle 7	2018	150	Q_{tot} = -53.3 m^3/day
Idle Cycle 7	2018	30	None
Injection Cycle 8	2019	150	Q_{tot} = 133.3 m^3/day
Idle Cycle 8	2019	30	None
Pumping Cycle 8	2019	150	Q_{tot} = -53.3 m^3/day
Idle Cycle 8	2019	30	None

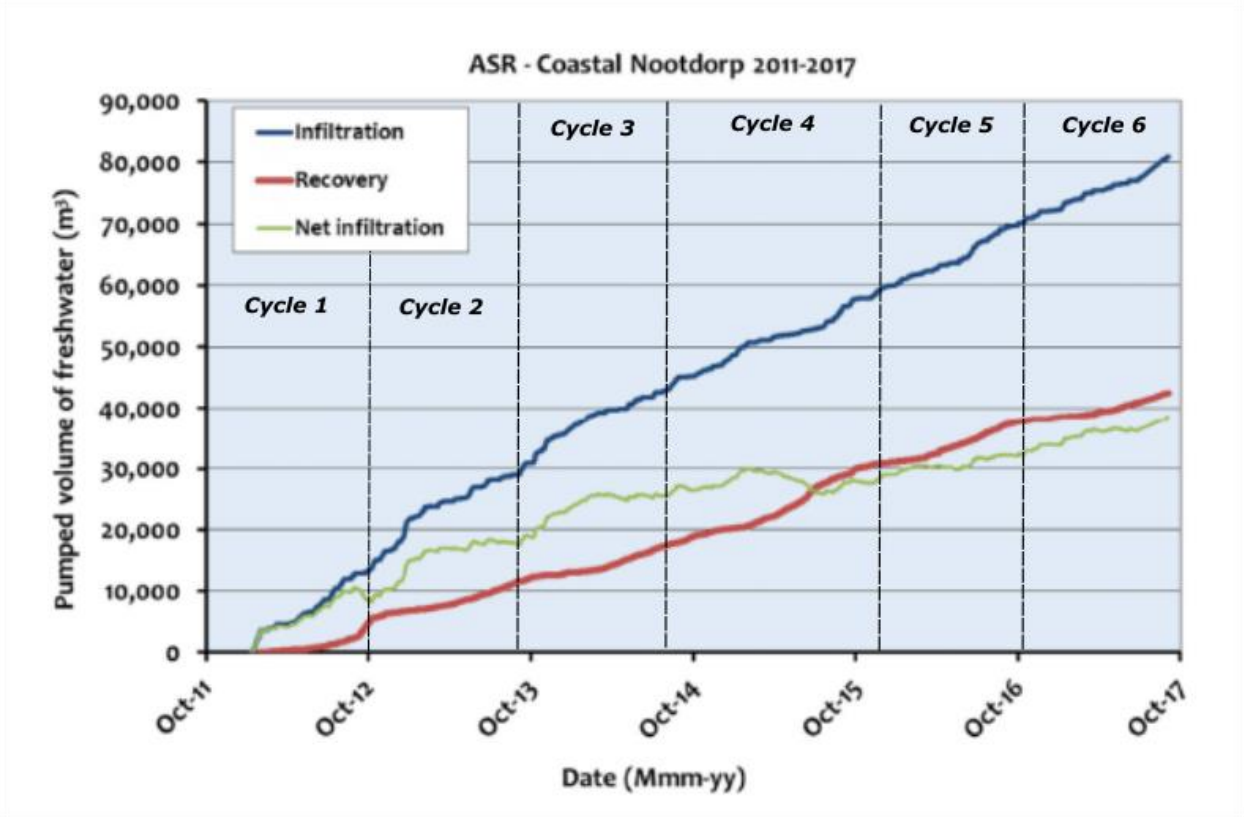

Figure 6: A detailed graph showing the volumes of water that have been infiltrated and recovered at Nootdorp. The data from this graph is the pumping data that was used in order to simulate the density-dependent flow at Nootdorp and help validate the model [Zuurbier et al., 2017].

2.4.3 PHT3D Model

Modeling the reactive transport that occurred at the Nootdorp site was done using the PHT3D computer code. PHT3D is a reactive transport computer program that couples the MT3DMS and PHREEQC [Parkhurst and Appelo, 1999] computer codes. In order to do this with FloPy, input files that were generated from the SEAWAT computer code were modified. These modifications allowed for the PHT3D code to use the density-dependent flow created by SEAWAT for the reactive transport simulations.

Three constant sink/source boundaries were placed in the same positions as the constant head boundaries in the model (Figure 5). Table 6 lists the constituents that were chosen for the reactive transport simulations and their initial concentrations throughout the aquifer and in the injection water. Initial concentrations were based on the geochemical analysis done in Zuurbier et al., 2016. Calcite was selected as an equilibrium mineral and given a saturation index of 0.5, which is the average saturation index measured at the ASR-wells. Ferrihydrite ($Fe(OH)_3$) and Pyrolusite (MnO_2) were also selected as an equilibrium minerals with an SI of 0.0, while pyrite, rhodochrosite, and siderite were selected as kinetic minerals. The exchangers that were chosen include *Ca-X, Na-X, K-X, Mg-X, Fe-X, Mn-X,* and *NH_4-X*. For mineral and exchanger compositions, concentrations were corrected for the axial-symmetric configuration [Wallis et al., 2013].

The standard PHT3D database was used to simulate the reactions occurring at Nootdorp. Within the standard database, additions were made in order to avoid convergence errors during simulations of redox processes. The kinetic rate reactions for the rhodochrosite and siderite dissolution were also added. The data that was produced from the simulations were then all post-processed in Python. Four scenarios were then simulated with the resulting reactive transport model: (1) a base simulation with 2 extra cycles (Table 5), (2) a simulation where the injection water was equilibrated with 5 mM of calcite, (3) a simulation in which the well is decommissioned (no pumping or injection) in Cycles 7 and 8, and (4) a simulation in which the injection water contained an O_2 concentration of 0.41 mM (max observed O_2 in the injection water) for the entire simulation. By understanding the effect injection water composition, injection/pumping schemes, and decommissioning have on the dominant processes at Nootdorp, a further understanding of the impact MPPW-ASR has on coastal aquifers can be attained.

3.4.4 Model Assumptions

To model the density-dependent flow at the ASR-site and to assess the buoyancy effects occurring at Nootdorp, it was assumed that there is no regional lateral background flow. Assuming no regional lateral background flow or a weak regional flow field is required to reasonably assume an axial-symmetric configuration [Langevin, 2008]. At the Nootdorp site, the regional background flow is considered negligible, therefore assuming axial-symmetry in the model is justified. While only buoyancy effects are taken into consideration, the non-continuous clayey interval located in HU-e was not included in the model and could potentially affect the flow created through buoyancy effects by preventing upconing of the intruding brackish water. It was also assumed that for each hydrogeological unit and geochemical unit, the composition of those units are laterally homogenous. The temperature for the reactive transport model was set to 10.5 ^{o}C (the average temperature measured at the monitoring wells) and did not vary.

Table 6: List of the constituents and initial concentrations that were used in running the reactive transport model. Concentrations were input into the model for each row based on the concentrations observed at the monitoring wells in Zuurbier et al., 2016.

Parameter	Units	Initial Concentration at the MW screens				Injection Concentration
		S1	S2	S3	S4	
Ca^{2+}	mmol/L	4.0	4.5	5.4	7.0	0.2
HCO_3^-	mmol/L	14.4	17.3	21.0	0.6	0.6
Cl^-	mmol/L	3.2	10.0	21.3	27.6	0.1
Na^+	mmol/L	6.6	12.0	19.7	25.8	0.1
K^+	mmol/L	0.3	0.4	0.6	0.9	0.01
Mg^{2+}	mmol/L	0.8	1.3	2.0	2.8	0.02
Fe^{2+}	µmol/L	469	335	245	258	0.2
Mn^{2+}	µmol/L	19	19	22	30	0.1
O_2	mmol/L	0.0	0.0	0.0	0.0	0.32
SO_4^{2-}	mmol/L	0.0	0.0	0.0	0.0	0.03
NH_4^+	mmol/L	1.2	1.6	1.2	1.0	0.0
pH	[-]	6.9	7.0	7.0	7.0	7.5

3. Results

3.1 Geochemical Analysis

3.1.1 Observed Trends for Na^+

Throughout the Nootdorp ASR pilot, concentrations for Na^+ at the ASR and monitoring wells were consistently checked due to the low limit set for Na^+ (0.5 mM). During Cycles 5 and 6, Na^+ concentrations at AWS1 and AWS2 had mostly become equal with observed Cl^- concentrations in the relatively unmixed freshwater (Figure 7). Only one stage of recovery in Cycle 5 was met with elevated Na^+ concentrations relative to Cl^- concentrations at AWS1 and AWS2, but concentrations remained below the desired limits. The same samples with elevated Na^+ concentrations also had a slightly positive base exchange index (BEX), indicating that recent freshening had occurred (Table 4). Elevated Na^+ concentrations relative to Cl^- were not encountered in Cycle 6 at either of the recovery wells. At AWS3 and AWS4, concentrations of Na^+ were generally lower than Cl^- concentrations during salinization of the deeper aquifer. While Na^+ concentrations at AWS3 were still below the 0.5 mM limit, concentrations at AWS4 reached up to ~25 mM during stages of recovery. The monitoring wells located in the shallower aquifer (MW1S1 and MW1S2) showed an enrichment of Na^+ upon injection at the beginning of Cycle 5, but concentrations were below the set limit. Comparing the data from Cycle 1 to Cycles 5 and 6 at the monitoring wells 5 m away, concentrations measured at MW1S1-MW1S3 showed an overall decrease (Figure 7). In Cycle 1, concentrations for Na^+ regularly exceeded the set limit at all the monitoring wells. Observed data points from Cycles 5 and 6 though are all below the limit of 0.5 mM for Na^+. While MW1S1-MW1S3 are linked with decreasing concentrations for both Na^+ and Cl^-, repeated salinization of the deeper monitoring well, MW1S4, continues to deteriorate the water quality in Cycles 5 and 6.

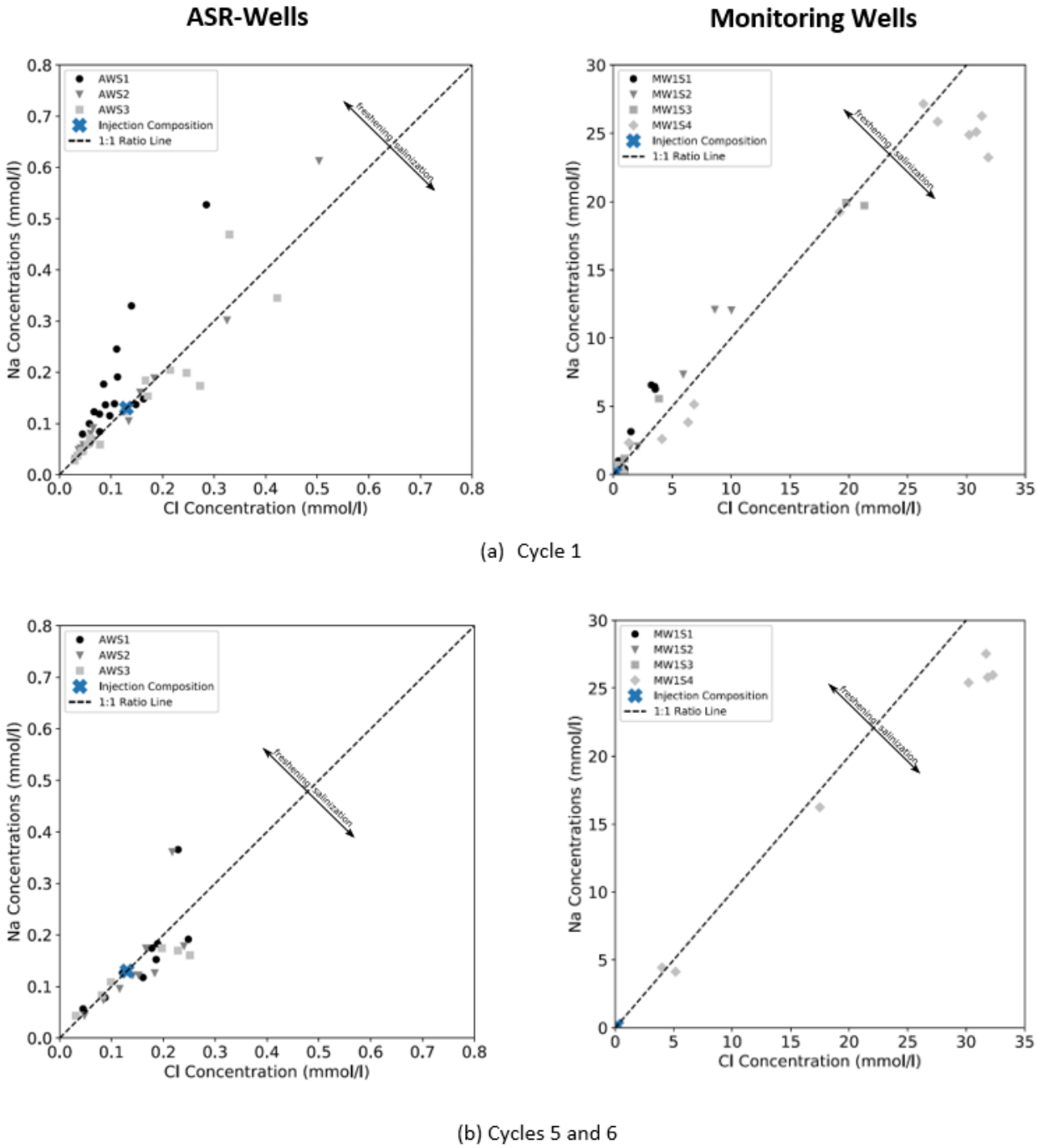

Figure 7: Cl vs. Na concentrations during the first cycle (a) and the fifth and sixth cycle (b). (a) Represents the higher concentrations seen in the beginning of the ASR operation while (b) demonstrates the decrease in concentrations for both species after 5 years of operation.

3.1.2 Observed Trends for Fe^{2+} and Mn^{2+}

In the Nootdorp aquifer, Fe^{2+} and Mn^{2+} initially are present in high concentrations throughout the aquifer (ranging from ~245-469 µM for Fe^{2+} and 19-30 µM for Mn^{2+}). During Cycle 1, an undesirable

arrival of Mn^{2+} at AWS1 and AWS2 was consistently occurring (~3-10 µM). Simultaneously, the Fe^{2+} concentrations at the recovery wells were typically lower than that of the Mn^{2+} concentrations. These observed concentrations contradicted the initial concentrations of both species in the ambient water, where Fe^{2+} concentrations were ~10x higher than the Mn^{2+} concentrations. Cycle 2 showed an overall decrease in the concentrations for both species at the recovery wells when compared to Cycle 1. It should be noted that during this cycle, the injection scheme was adjusted to promote subsurface iron removal (SIR). Inversely, both showed a relative increase in concentration at AWS3 and AWS4 during recovery in comparison to the previous cycle. Observations from the monitoring wells indicated there was a small decrease in concentrations for both species from Cycle 1 to Cycle 2 in the top three wells but were still above the desired limits for majority of the points. This indicated that the risk of exceedance was still present for the system.

The data observed in Cycles 5 and 6 reached detection limits for both species (0.8 µM for Fe^{2+} and 0.09 µM for Mn^{2+}) at the ASR wells for nearly each date. However, Mn^{2+} concentrations at AWS2-AWS4 were still elevated in some samples. One sample during Cycle 5 at AWS4 had a Mn^{2+} concentration that reached 329 µM. In Cycle 6, one sample from AWS2 contained 1.5µM of Mn^{2+}, as well as an Fe^{2+} concentration of 3µM. This same sample was marked with a neutral BEX, indicating that freshening had been completed (Table 4).

3.1.3 Mobilization of Fe^{2+} and Mn^{2+}

During Cycles 1 and 2, elevated Mn:Fe concentrations were observed. Assessing the data in Cycles 5 and 6 demonstrated that the same trends were still present (Figure 8). Figure 8 presents the Fe^{2+} and Mn^{2+} concentrations plotted together with mixing lines and points representing the ambient water concentrations at AWS1 and AWS4 for reference. While for most samples, both species were stopped at a detection limit at the ASR-wells, instances of an increased Mn:Fe ratio were still observed at AWS4. At the ASR-wells, most data points plotted are unmixed water based on low Cl^- concentrations and should not plot along the mixing lines. However, one sample at AWS4 during Cycle 5 contained a Mn^{2+} concentration of 329 µM (not shown), as well as a high Cl^- concentration (~21 mM). The same sample also contained an Fe^{2+} concentration below the detection limit.

It was observed that in Cycle 1, the data at MW1S1 and MW1S2 plotted along a mixing line, but data tended to move towards higher Mn:Fe ratios during the subsequent Cycles. These trends are indicative of ongoing MnO_2 reduction by Fe^{2+}, leading to the elevated Mn:Fe ratios seen at the ASR-wells and monitoring wells (Table 4). With the consumption of 2 mol of Fe^{2+} for the production of 1 mol of Mn^{2+}, plotting the data with a 1:2 (Mn:Fe) ratio line shows that Fe^{2+} concentrations are lower than expected if just MnO_2 reduction was occurring (Figure 8). Likely, other processes, such as oxidation, in combination with MnO_2 reduction are leading to decreased Fe^{2+} trends, while the elevated Mn^{2+} concentrations are due to MnO_2 dissolution at the monitoring wells.

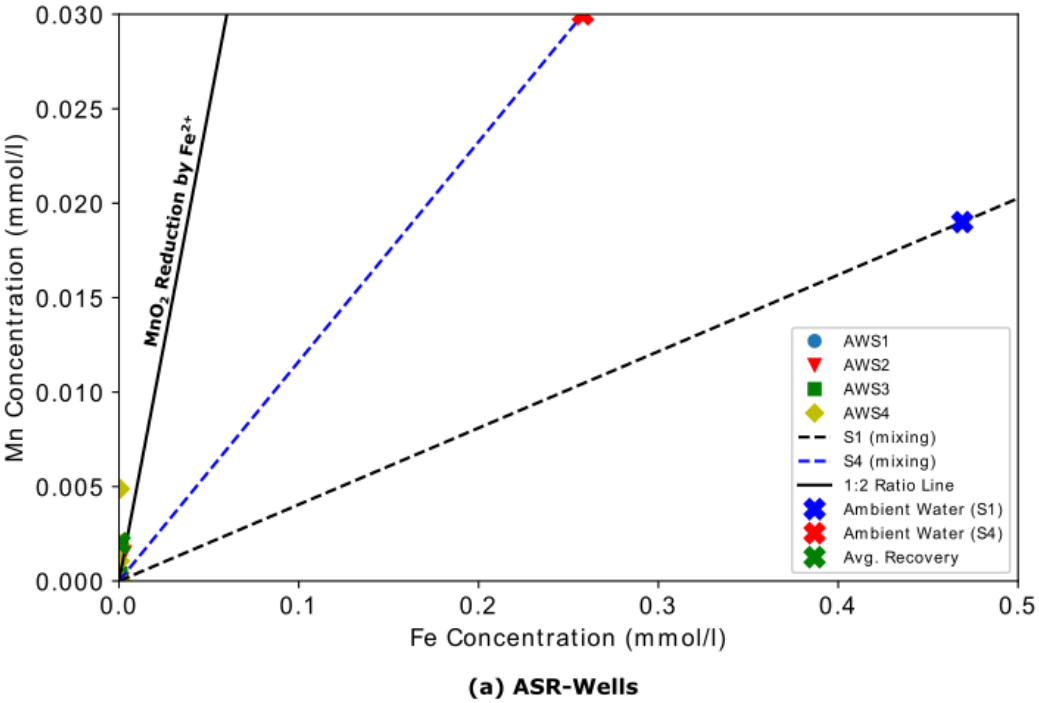

(a) ASR-Wells

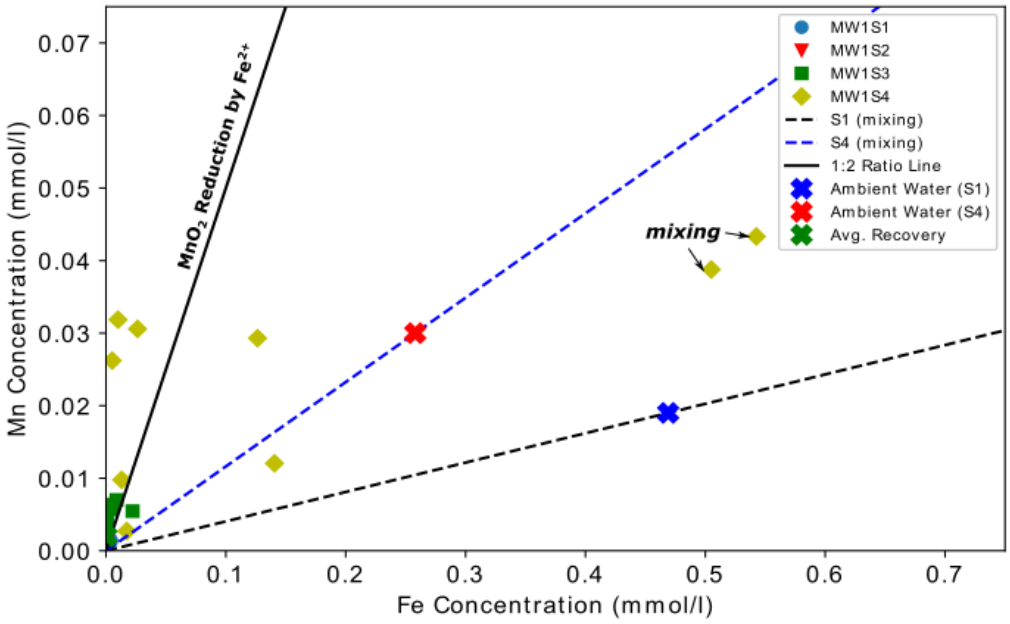

(b) Monitoring Wells 1

Figure 8: (a) Iron versus Manganese concentrations observed at the ASR-wells and (b) at the first monitoring well 5m away. Compared to previous cycles, Cycles 5 and 6 are met with higher Mn:Fe ratios, but lower concentrations for both species overall. A 1:2 ratio line was added in order to represent ongoing MnO_2 reduction.

3.1.4 Equilibrium Calcite Dissolution

In the target aquifer, carbonates are present in considerable amounts, mainly in the upper three geochemical units (GUI-III: ~5% weight). To investigate the extent of dissolution of carbonates throughout the ASR-pilot, Ca^{2+} concentrations were plotted against HCO_3^- concentrations (Figure 9). In Figure 9, Ca^{2+} and HCO_3^- concentrations generally followed a ±1:2 ($Ca:HCO_3$) ratio line, which represents equilibrium calcite dissolution for varying CO_2 pressure (Table 4). During Cycle 1, low Ca^{2+} concentrations relative to HCO_3^- concentrations at AWS1 were observed. These samples were typically accompanied with positive BEX values, indicating that freshening had occurred (Table 4). At AWS3, samples contained elevated Ca^{2+} concentrations and were accompanied by slightly positive BEX values. While a positive BEX is typically met with lower Ca^{2+} concentrations due to freshening (retardation), it is possible that the elevated Ca^{2+} concentrations relative to the HCO_3^- concentrations are due to calcite dissolution and proton buffering upon pyrite oxidation [Hartog et al., 2002] (Table 4).

While some points followed along the ratio line during Cycles 5 and 6, the Ca^{2+} concentrations were typically elevated in samples taken from the upper three ASR-wells. These elevated Ca^{2+} were nearly all marked with a slightly positive BEX values. PHREEQC batch reaction modeling showed that through equilibrium dissolution of calcite alone, a maximum value of 0.27 mM of Ca^{2+} could be produced [Zuurbier et al., 2016]. The elevated Ca^{2+} concentrations cannot be fully explained by the injection water composition and equilibrium dissolution. Likely, the combination of equilibrium dissolution and proton buffering by pyrite oxidation is what leads to the observed Ca^{2+} concentrations seen in Cycles 5 and 6.

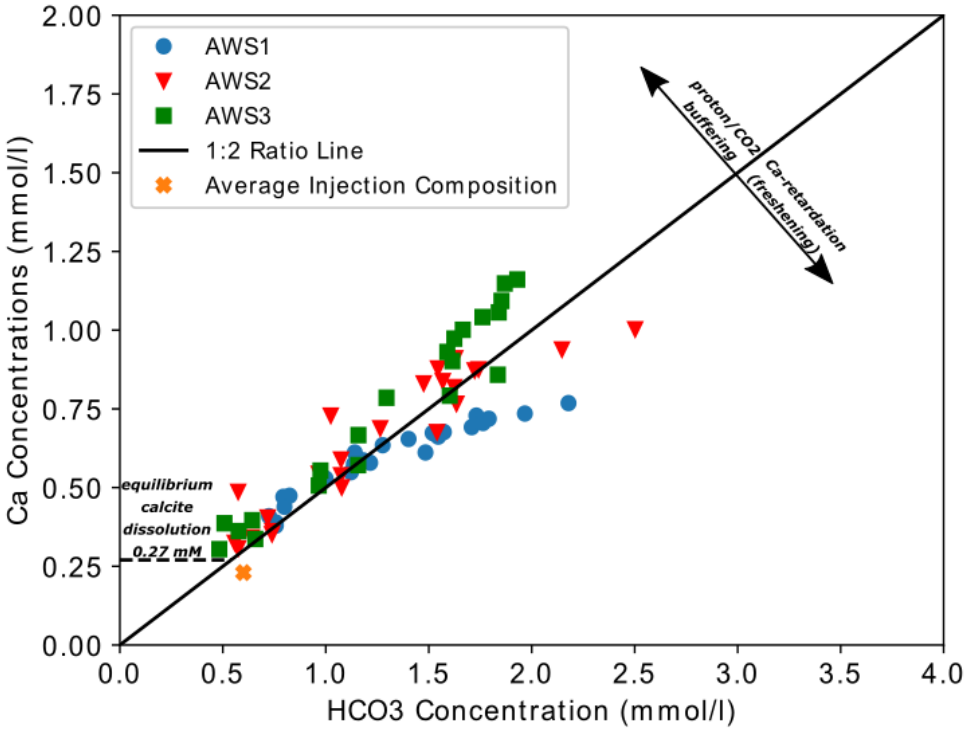

Figure 9: Ca^{2+} concentrations vs. HCO_3^- concentrations observed for all Cycles of the ASR-pilot. The observed concentrations for Ca are higher than predicted values for equilibrium calcite dissolution. Injection of Ca also does not explain the concentrations indicating other processes are producing the higher concentrations.

3.1.5 Conservative SO_4^{2-}

SO_4^{2-} concentrations that were observed in the aquifer upon injection indicated that the pyrite oxidation was occurring (Table 4). To assess whether SO_4^{2-} could be considered conservative, SO_4^{2-} was plotted with Cl^-. Because Cl^- is considered a conservative tracer for the brackish water, a negative trend between Cl^- and SO_4^{2-} could mean that SO_4^{2-} is a conservative tracer for the freshwater. In figure 10, the SO_4:Cl concentrations had a negative correlation at AWS4. The observed concentrations follow mixing lines representing expected values of SO_4:Cl upon maximum and average O_2 concentrations consumed by pyrite. Points at the top-most three wells show near-zero values for Cl^-, while SO_4^{2-} values range from 0.03 mmol/L (the average injection concentration for SO_4^{2-}) to 0.27 mmol/L. The low Cl^- values in the top three wells indicate that these points are unmixed injection water. The SO_4^{2-} values observed at the ASR-wells are nearly all within the range of expected values based on the maximum and minimum observed O_2 concentrations in the injection water (0.21 - 0.41 mM), which should produce values of SO_4^{2-} up to 0.25 mM based on the reaction stoichiometry in table 4. Two points at AWS3 and AWS4 both plot outside of the expected values for SO_4^{2-} though. This is potentially from further oxidation of pyrite by NO_3^- (Table 4), where only 0.5 mM of NO_3^- is required to produce the 0.36 mM of SO_4^{2-} observed at AWS4. At the monitoring wells MW1 (5m away) and MW2 (15m away), concentrations observed in the deeper intervals of the well showed to follow the same negative trend but did not plot directly on the lines of expected values at well-screens 1 and 4. Because the concentrations for Cl^- and SO_4^{2-} at AWS4 follow the mixing lines for varying O_2 consumption by pyrite, this indicates that SO_4^{2-} can be considered conservative in the system.

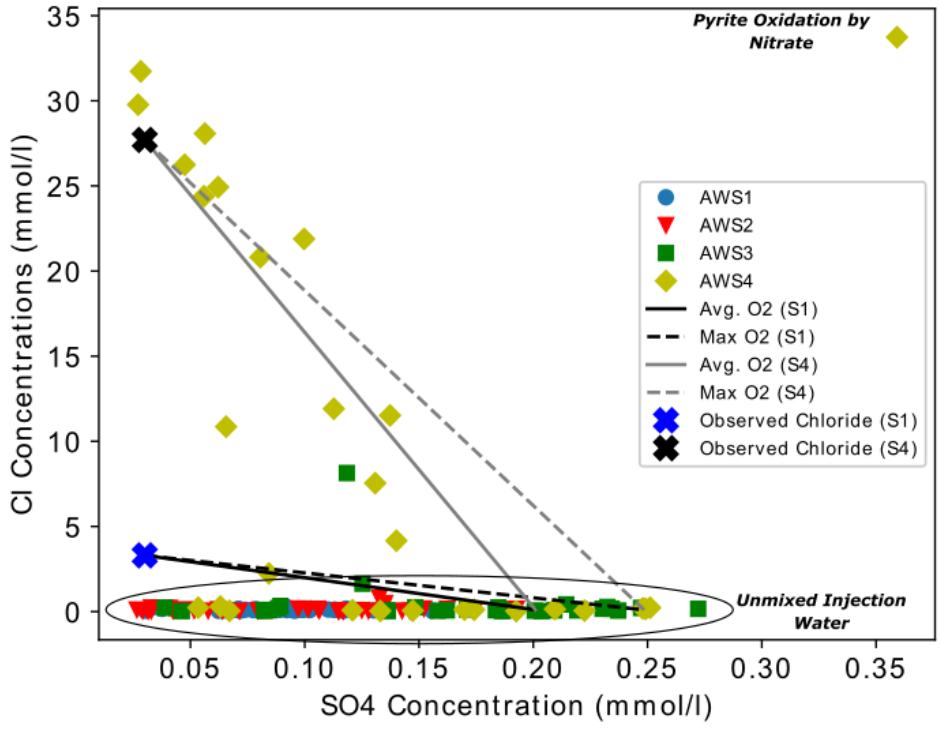

Figure 10: SO4 vs. Cl concentrations. In order to assess whether SO4 is conservative, lines of expected values for SO4:Cl ratios were plotted with the observed data points. One point at AWS4 shows much higher SO4:Cl ratio than other observed points. This point was seen with a negative BEX and after an increase in NO_3, which potentially caused the high SO_4 value through oxidation of pyrite by nitrate.

3.1.6 Analysis of Pyrite Oxidation

3.1.6.1 Extent of pyrite oxidation

Geochemical analysis previously done at Nootdorp showed that pyrite was present throughout the aquifer. The largest amounts of pyrite were located in GU-III and IV (1.05% weight and 0.90% weight), while units GU-I, II, and V contained lesser amounts (0.06% weight, 0.09% weight, and 0.28% weight). Pyrite oxidation occurring in the aquifer was indicated by a presence of SO_4^{2-} upon injection of the oxic freshwater. Table 7 lists the calculated percentages of oxygen consumption by pyrite-oxidation at each monitoring well during Cycles 1, 2, and 5 of MPPW-ASR. These Cycles were chosen because ample data was available for each Cycle, whereas during Cycle 6, too little data could be used for this calculation. At MW1S1 and MW1S2, 48% and 18% of oxygen was calculated to be consumed by pyrite-oxidation during Cycle 1. Alternatively, 58% and 68% of oxygen was consumed by pyrite-oxidation at MW1S3 and MW1S4 [Zuurbier et al., 2016]. This is likely due to the geochemically heterogeneous nature of this aquifer, where SOM and other dissolved constituents are likely to consume oxygen preferentially over pyrite. In Cycle 2, nearly all oxygen injected into the deeper aquifer was consumed via pyrite-oxidation. Cycle 5 demonstrated that majority of the oxygen was no longer being consumed by pyrite at MW1S3 and MW1S4, but ongoing oxidation of pyrite was occurring throughout the length of the aquifer.

3.1.6.2 PHREEQC modeling of pyrite oxidation

Further PHREEQC modeling was done to investigate the amount of pyrite that would be remaining in the bottom most well (MW1S4) after Cycle 5. An initial solution containing pyrite, ferrihydrite, calcite, and pyrolusite was created based on observed concentrations and brought into contact with oxygen-rich water, simulating injection. The simulation ran for the length of each Cycle. With an initial concentration of 0.117 M, the simulation of 5 years of pyrite oxidation showed that 0.0908 M would be remaining. This is a $\Delta C = -0.0262$ for pyrite oxidation, where 22.4% of the pyrite at MW1S4 has been dissolved through oxidation. This dissolution could lead to a lower rate of oxidation of pyrite based on the kinetic reaction (equation 3) , where the change in pyrite mass is taken into account.

Well	Cycle 1	Cycle 2	Cycle 5
MW1S1	48%	33%*	42%
MW1S2	18%	23%	44%
MW1S3	58%	108%	60%
MW1S4	68%	98%	36%

*Table 7: Amount of oxygen consumed due to pyrite oxidation per cycle at each of the monitoring wells. A large decrease in consumption is observed at MW1S4 between Cycle 2 and Cycle 5, while an increase is occurring at MW1S2. This indicates that different processes are most likely consuming oxygen preferentially during different Cycles. *Based on observed concentrations at AWS1. Values from Cycles 1 and 2 from Zuurbier et al., 2016.*

3.1.7 Observed Trends for As and Zn^{2+}

Trace metal concentrations (mainly Zn^{2+} and As) have been observed throughout the Nootdorp pilot (Figure 11). After freshening in Cycle 1, Zn^{2+} concentrations decreased at the monitoring wells 5m away. The beginning stages of recovery at the ASR-wells showed decreased concentrations at AWS1-AWS3, but elevated concentrations at AWS4 (~0.94 µM). Later stages of recovery were met with increasing Zn^{2+} concentrations at all four ASR-wells, but concentrations decreased at the end of Cycle 1 at the primary recovery wells. The injection composition of Zn^{2+} was highly variable, containing concentrations ranging from 0.05 µM to 0.4 µM. Arsenic concentrations showed an increase at the monitoring wells 5m away during injection, especially at MW1S3 and MW1S4 in the deeper aquifer interval where initially concentrations were virtually 0 µM. During later stages of recovery, an increase in As concentrations was observed at AWS1 and in the recovered water, but decreased at the end of the cycle. Virtually no As was detected in the recovered water at the end of Cycle 1.

Zn^{2+} concentrations in Cycle 2 continued to exhibit decreasing concentrations at the MW1 well screens during injection. The ASR-wells also showed a general decrease during injection. During stages of recovery, increases in concentrations at the recovery wells were observed, but no concentrations for Zn^{2+} exceeded the injection amounts. At the bottom of the ASR-well, Zn^{2+} concentrations showed an increase during later stages of recovery that were ~10x higher than concentrations observed at the MW1 screens. Elevated As concentrations (~0.12 µM) were observed during late stages of recovery at AWS1, but concentrations were generally lower than in Cycle 1. AWS2-AWS4 were met with non-detectable limits for As at many points, mostly during freshening. Data for Cycles 5 and 6 showed Zn^{2+} concentrations stayed below the detection limit (<0.3 µM) at AWS1 and AWS2, except in one sample where elevated concentrations were observed (1.9 and 3 µM). Increased concentrations were observed at AWS3 and AWS4 during injection, but a decrease was seen during recovery. Arsenic concentrations seemed to continue decreasing over time, staying below 0.1µM at AWS1-AWS3 for all of Cycles 5 and 6. Only at MW1S4 were elevated concentrations of As observed during Cycles 5 and 6.

3.1.8 Trace Metal Mobilization

Geochemical analysis of the sediment at Nootdorp showed that As and Zn^{2+} were potentially present in pyrite samples throughout the length of the aquifer. As:FeS_2 ratios were highest in GU-I at the top of the aquifer and the lowest ratio was in GU-IV (0.006 (-) and 0.001 (-) respectively) (Figure 3). Zn^{2+}:FeS_2 were also highest in GU-I with a ratio of 0.029 (-) and lowest in GU-IV with a ratio of 0.001(-). The release of SO_4^{2-} to release of As and Zn^{2+} were assessed with the sediment ratio lines based on the elemental sediment composition (Figure 12).

Only at AWS1-AWS3, concentrations for both Zn^{2+} and SO_4^{2-} plot on the sediment ratio line representing the Zn:FeS_2 ratio at GU-V (at MW1S4). Samples from AWS4 that plot above either sediment ratio lines all occur during times of salinization and have higher Cl^- concentrations, which also explains why there is a lower SO_4^{2-} composition at those points. Two points from AWS1 and AWS2 also plotted above the two sediment ratio lines. The samples that these points were taken from also have a slightly positive BEX and are a part of the same samples that contained elevated Na^+ concentrations seen in figure 7. For As, only at AWS1 and AWS2 did points plot onto either of the sediment ratio lines (Figure 12). Assuming that SO_4^{2-} acts conservatively, this result suggests that pyrite could a source for As and Zn^{2+}. This assumption also indicates that As is potentially affected by surface complexation, as this could be the reason why As concentrations are lower than expected based on release through pyrite oxidation.

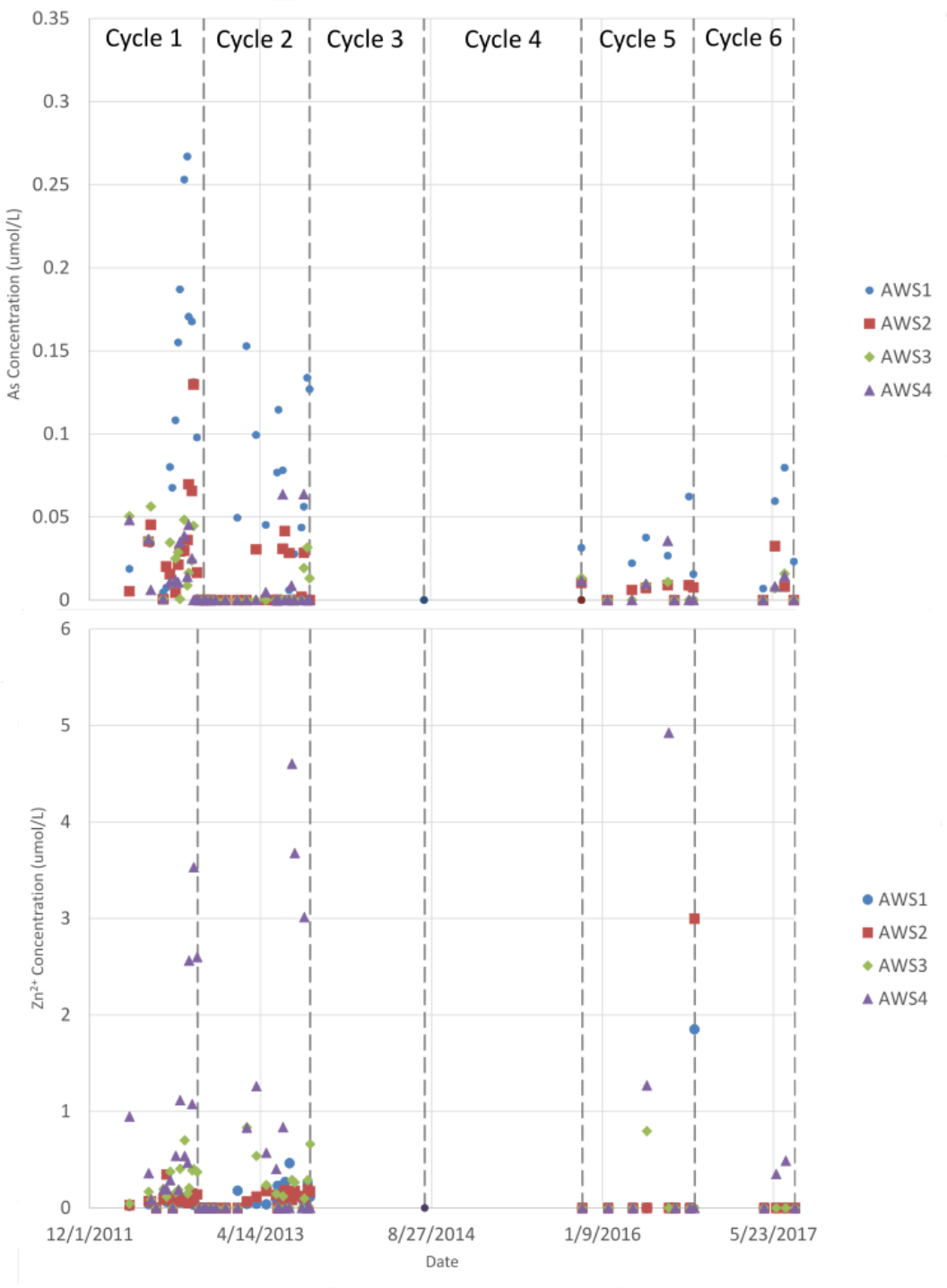

Figure 11: Evolution of Arsenic (Top) and Zinc (bottom) concentrations at the ASR-wells, listed by Cycle. Increases in both trace metals were observed in Cycle 1, but overall have decreased after multiple ASR cycles.

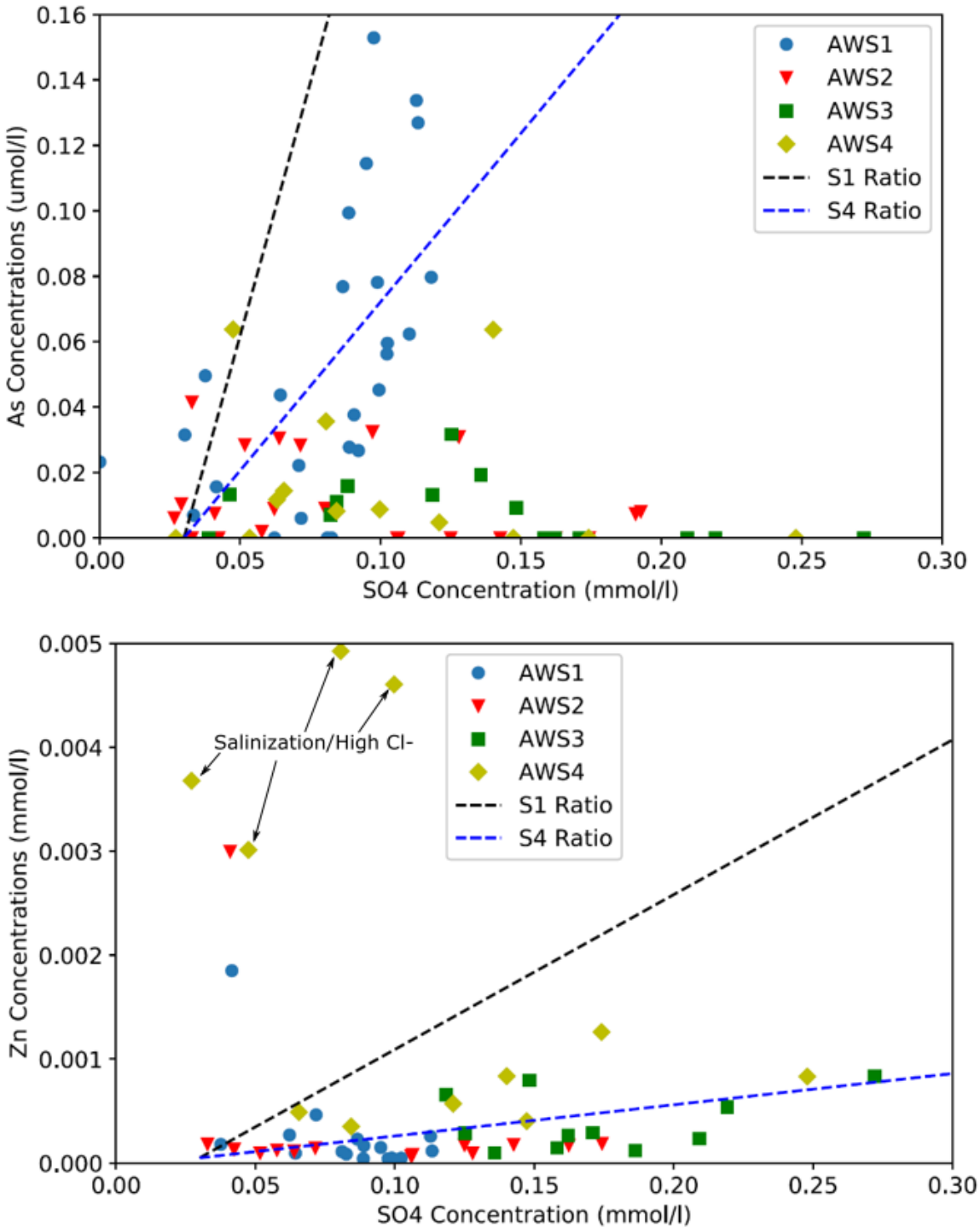

Figure 12: Arsenic vs. sulfate (left) and zinc vs. sulfate (right). The observed As concentrations are lower than expected when looking at the ratio line for As:SO4 release from pyrite. The right graph demonstrates many points falling along the ratio line for Zn:SO4 release from the bottom of the well.

3.2 Modeling of Dominant Processes

3.2.1 Flow Validation

Assessment of modeling the flow that is observed at the Nootdorp site was done by plotting simulated concentrations for Cl^- with the observed concentrations of Cl^- (Figure 13). The simulated results at both AWS1 and AWS2 were generally higher than the observed results, where the simulated Cl^- concentrations would not drop below 0.1 mM, which is the average Cl^- composition found in the injection water. The trends that were observed at both recovery wells were reproduced throughout the ASR-pilot, except during recovery at AWS2 during Cycle 1 where an observed increase in Cl^- was not shown by the model. During Cycle 4, a large increase in Cl^- is simulated at both wells, as well as at the monitoring wells (Figure 13). Geochemical data points from November of 2015 show that the electric conductance was low during this date, as well as a slightly positive BEX for both wells. This increase in Cl^- at nearly all wells is potentially due to upconing of the ambient brackish water. This phenomenon is not observed at the Nootdorp site, possibly because the non-continuous clayey interval located in the deeper monitoring wells (MW1S3 and MW1S4) (Figure 4) prevents upconing of brackish water to these wells.

At AWS3 and AWS4, the observed trends were also reproduced. At AWS4, Cl^- concentrations observed increasing during times of recovery was shown by the model, but simulated concentrations tended to be lower than the observed concentrations. The trends seen from data at the monitoring wells were reproduced for MW1S1, MW1S2, and MW1S4. The model was not able to simulate the observed trends at MW1S3 though, where the model simulated increases in Cl^- that were not occurring at the site. This is also likely due to the non-continuous clayey interval, which is located at the same position as MW1S3. Overall, the model was able to simulate the general trends that were observed with respect to conservative chloride transport.

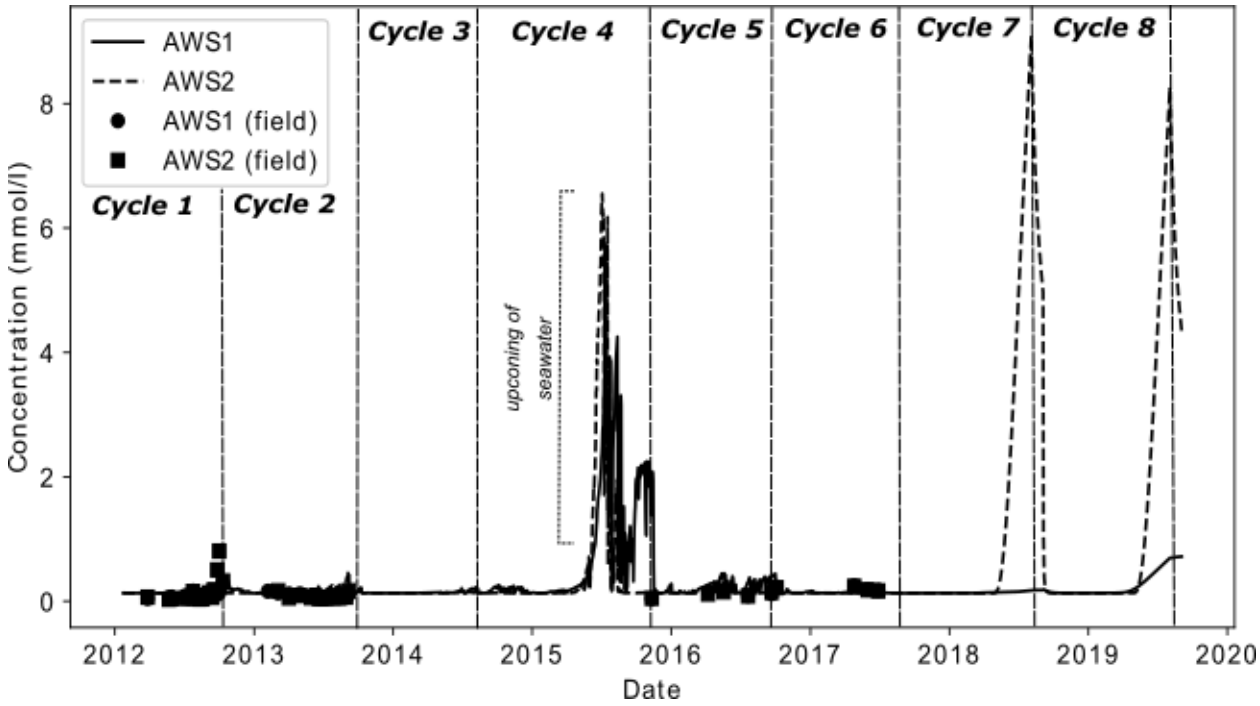

Figure 13: Observed Chloride concentrations plotted with simulated Chloride concentrations at AWS1 and AWS2. Observed results plot along the simulated results, but simulated results tend to be slightly higher than the observed concentrations.

3.2.2 Cation-Exchange and Equilibrium Calcite Dissolution

3.2.2.1 Simulation of observed trends in Na^+

With the addition of equilibrium cation-exchange reactions and equilibrium calcite to the PHT3D model, the simulated Na^+ concentrations were plotted with the field data (Figure 14). Overall, the field data for Na^+ plotted along the simulated concentrations performed via the model and general trends observed in the field were reproduced for the ASR wells and the monitoring wells. The model showed that at the primary recovery well, AWS1, Na^+ concentrations were elevated with respect to Cl^- concentrations during the initial cycles of the pilot, becoming nearly equal in Cycles 5 and 6. This result matches that of the field data seen in figure 6a. Only during the recovery stages in Cycle 4 are simulated Cl^- concentrations higher than Na^+ concentrations, indicating the arrival of the ambient water to the ASR-wells. During Cycle 7 and Cycle 8, Na^+ concentrations at AWS1 were continuously elevated with respect to Cl^-, reaching concentrations up to ~1 mM in Cycle 8. At AWS2, Na^+ concentrations increased to ~3.5 mM during both Cycle 7 and Cycle 8.

3.2.2.2 Effects of decommissioning the well for Na^+

Upon the simulated decommissioning of the well, Na^+ concentrations started to gradually increase at both AWS1 and AWS2 (Figure 14). During Cycles 7 and 8, Na^+ concentrations only increased to ~0.2 mM at AWS1 but increased to ~2.2 mM at AWS2. Similar trends were observed at the deeper well screens, where concentrations increased to ~20 mM at both AWS3 and AWS4 during Cycle 7. In Cycle 8, Na^+ concentrations remained the same as in the previous cycle.

3.2.2.3 Assessment of equilibrium cation-exchange and calcite dissolution on Ca^{2+}

While the trends and concentrations for Na^+ were realized by the model, the field data for Ca^{2+} did not plot along the simulated concentrations, as simulated concentrations tended to stay at ~0.37 mM. This relatively constant concentration for Ca^{2+} remained below the data points observed in the field for each of the three ASR-wells. During the geochemical analysis, it was indicated that calcite dissolution in combination with proton buffering and CO_2-production (Table 4) is what is leading to the elevated Ca^{2+} concentrations (Figure 9). Through modeling equilibrium cation-exchange and equilibrium calcite dissolution, the lack of simulated Ca^{2+} in the model further indicates this interpretation.

3.2.2.4 Effects of cation-exchange on Fe^{2+} and Mn^{2+}

Upon the addition of equilibrium cation-exchange, the effect that it and mixing had on Fe^{2+} and Mn^{2+} was assessed. At AWS1-AWS3, observed Fe^{2+} concentrations were not plotted along the simulated lines for cation-exchange. Some Fe^{2+} data points plotted along the simulated mixing lines at AWS1, but this was not seen at the other two wells. Simulations just including cation-exchange and calcite dissolution showed that the Fe^{2+} concentrations remained at 0 M at all three wells throughout the entire simulation. Observed Mn^{2+} concentrations were consistently higher than simulated concentrations at AWS1 during Cycle 1 with cation-exchange added. During Cycles 2, 5, and 6 the observed concentrations were typically lower than that of the simulated results. No Mn^{2+} data points or trends were plotted or reproduced with mixing or cation-exchange.

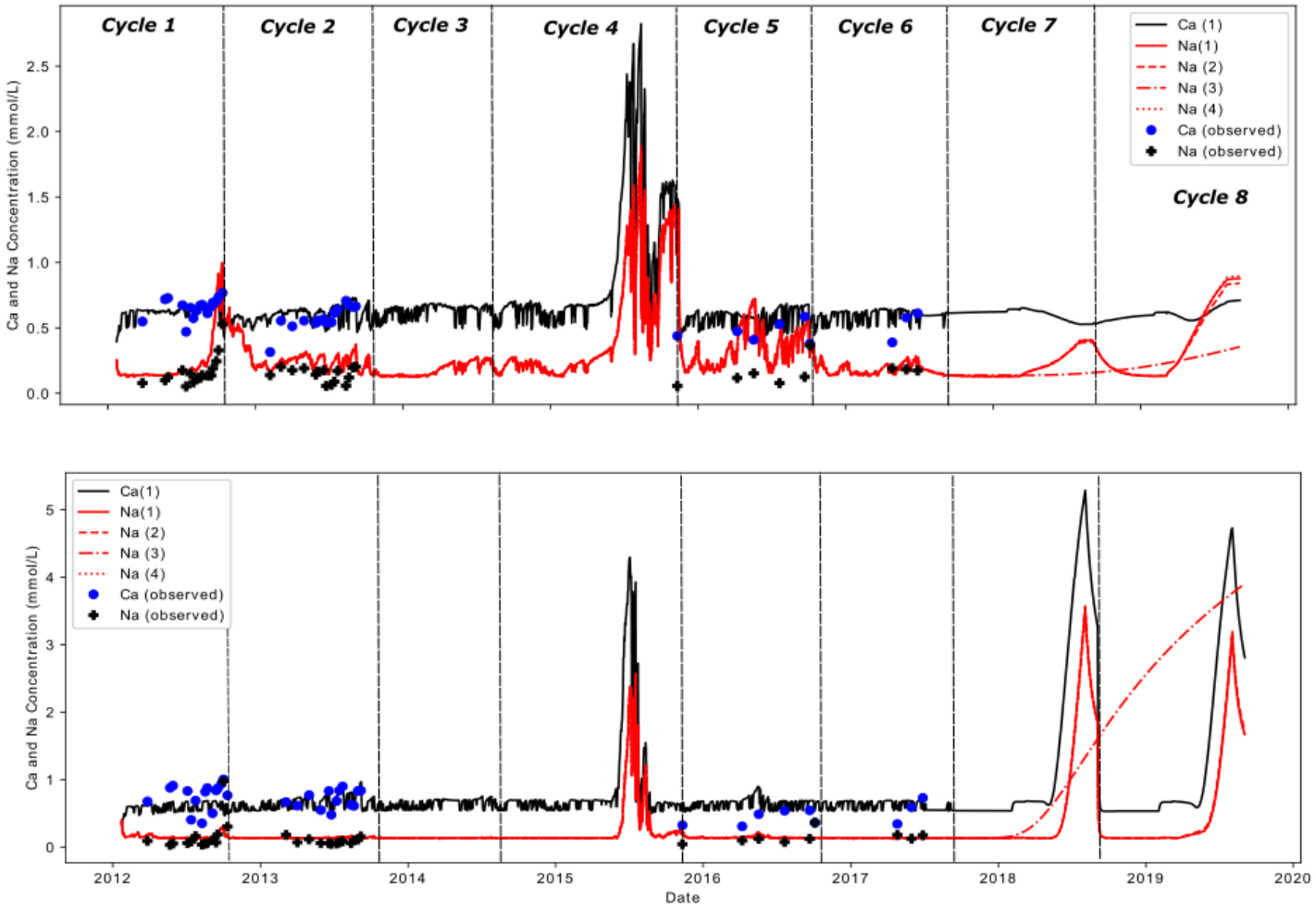

Figure 14: Simulated calcium(black) and sodium(red) concentrations for scenarios 1-4 (listed in section 2.4.3) plotted with observed calcium (blue circles) and sodium (black plusses) concentrations for AWS1 (top) and AWS2 (bottom).

3.2.3 Kinetic Pyrite Oxidation

3.2.3.1 Reproduction of Ca^{2+} concentrations observed at Nootdorp

With equilibrium cation-exchange and equilibrium calcite dissolution included in the reactive transport model, the simulated Ca^{2+} concentrations were typically lower than the observed concentrations throughout the entire simulation. When kinetic pyrite oxidation was included in the model, the simulated Ca^{2+} concentrations matched that of the observed concentrations seen at Nootdorp (Figure 15). During the geochemical analysis, it was suspected that calcite dissolution due to proton buffering upon pyrite oxidation was occurring (Figure 9). Through reactive transport modeling of pyrite oxidation at the Nootdorp site, this buffering process was further proven to be what is occurring at the site.

While Ca^{2+} concentrations and trends were simulated at each of the ASR-wells, the relative increase seen at AWS1 during recovery in Cycle 1 was not reproduced by the model. This indicated that other processes, such as proton buffering upon Fe^{2+} and Mn^{2+} oxidation or CO_2 buffering upon SOM oxidation (Table 4), were also responsible for calcite dissolution during this cycle. At AWS4, Ca^{2+} concentrations during recovery in Cycle 1 and Cycle 2 were generally higher than the model predicted. At the monitoring wells, Ca^{2+} trends and concentrations were also reproduced well with the addition of pyrite oxidation, except at MW1S3, where the non-continuous clayey interval is located.

3.2.3.2 Pyrite oxidation effects on SO_4^{2-} and Fe^{2+} concentrations

The addition of kinetic pyrite oxidation to the PHT3D model had a direct effect on Fe^{2+} and SO_4^{2-} concentrations. Where equilibrium cation-exchange and mixing simulated little to no Fe^{2+} at the ASR-wells, the addition of kinetic pyrite oxidation produced concentrations of Fe^{2+} up to 175 µM in the pyrite-rich intervals of the aquifer (GU-III, IV, and V) (Figure 3). Simulated Fe^{2+} concentrations were generally higher than Mn^{2+} concentrations at AWS1, AWS3, and AWS4 with pyrite added to the reaction network, contradicting the elevated Mn^{2+} concentrations observed at Nootdorp. At AWS2, the simulated Fe^{2+} concentrations stayed near 0 M, except during recovery during Cycle 1 and during recovery in Cycle 4.

The observed SO_4^{2-} points were plotted with the model results and showed that the kinetic pyrite oxidation was able to reproduce concentrations seen in the field (Figure 15). Figure 15 is a plot comparing the modeled SO_4^{2-} concentrations with the observed concentrations at the upper three monitoring wells (MW1S1-MW1S3) during the simulation that includes equilibrium cation-exchange, equilibrium calcite dissolution, and kinetic pyrite oxidation. In figure 15, most data seen for the modeled SO_4^{2-} is at ~0.14 mM. This is likely due to the constant O_2 injection concentration (0.32 mM), which would produce a SO_4^{2-} concentration of 0.17 mM based on the stoichiometry in table 4. The lack of SO_4^{2-} modeled based on this stoichiometry is likely due to some O_2 being used to oxidize Fe^{2+} to Fe^{3+}.

At MW1S1 and MW1S2, data typically plotted below the provided 1:1 ratio line, indicating that in the upper two wells, the model is producing SO_4^{2-} at a higher rate than what is observed. At MW1S3, data mostly plots above the ratio line, but other data points, all from Cycle 1, indicate higher rates of oxidation in the model at the same well. Without the inclusion of $Fe(OH)_3$, MnO_2, or SOM in the model, more O_2 can oxidize pyrite. It is also possible that the local clayey interval at this well prevents some O_2 from reacting with the surface of pyrite, while the model cannot simulate this. This could potentially explain why in Cycle 1, the model produced higher SO_4^{2-} concentrations than observed.

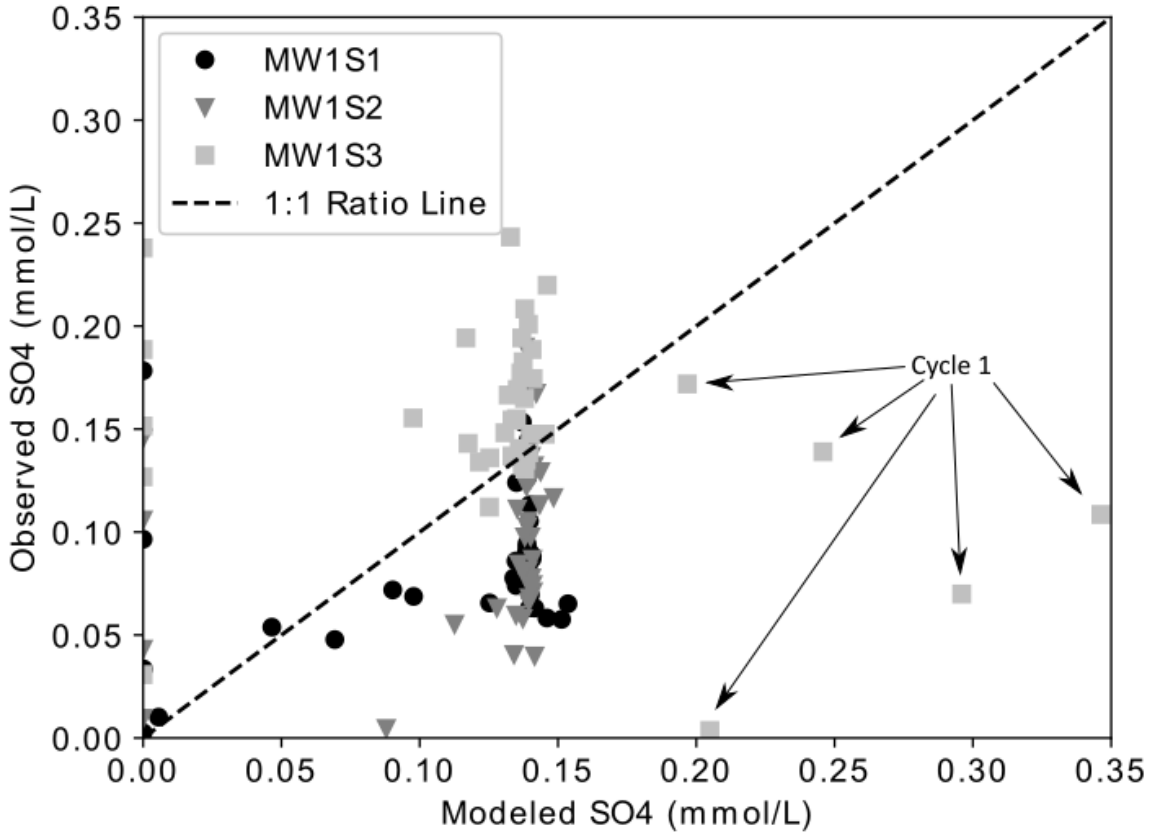

Figure 15: Observed SO_4^{2-} concentrations plotted with modeled SO_4^{2-} concentrations in order to compare how the model results match up with the observed points. Depending on the location of the well, the model output was either higher or lower than observed SO_4^{2-} concentrations. This likely has to do with the vertically heterogeneous nature of the aquifer, where dominant mineral interactions vary.

3.2.4 Fe-Mn-Minerals at Nootdorp

3.2.4.1 Equilibrium modeling with Fe^{2+}, Mn^{2+}, $Fe(OH)_3$, and MnO_2

Through geochemical analysis, the oxidation of Fe^{2+} and Mn^{2+} was suspected to be an important process for determining the fate of Fe^{2+} and Mn^{2+}. Therefore, the addition of $Fe(OH)_3$ and MnO_2 to the reactive transport model was required. It was assumed that both minerals were not present in the aquifer based on Nootdorp being a highly reduced environment before the first cycle of injection, and therefore had an initial concentration of 0 M. Upon the addition, the general trends for Fe^{2+} were realized at AWS1 and AWS2. At AWS3 and AWS4 though, simulated concentrations for Fe^{2+} regularly exceeded the observed concentrations during times of recovery and salinization. This is evident by the increases in Cl^- occurring simultaneously with the increase in Fe^{2+} at AWS4. During this time, dissolution of the newly formed $Fe(OH)_3$ minerals were also occurring. At the first set of monitoring wells, observed Fe^{2+} concentrations plotted along the simulated concentrations and the general trends were reproduced for MW1S1, MW1S2, and MW1S4. At MW1S3, the general trends for Fe^{2+} were not reproduced though. This is likely due to the non-continuous clay interval that is present at the location of this well.

The simulated Mn^{2+} concentrations were able to produce general trends that were observed at the ASR-site, but simulated concentrations were typically lower at all four of the ASR-wells due to oxidation of Mn^{2+} to MnO_2 (Table 4). When looking at the simulated concentrations for MnO_2 at AWS1, an increase from 0 µM to ~19 µM was observed during injection in Cycle 1. After completion of the injection phase, the concentration remained constant until the recovery phase in Cycle 1 began, where the MnO_2 concentration increased to ~25 µM. This increase in MnO_2 and lack of Mn^{2+} simulated by the model indicated that the reduction of MnO_2 by Fe^{2+} did not occur to the extent that was observed in the field (Table 4). Without the Fe-Mn-carbonates included in the model, there was not enough Fe^{2+} available to reduce MnO_2 in the upper aquifer interval and produce the undesirable arrival of Mn^{2+} at the recovery wells during Cycles 1 and 2.

3.2.4.2 Kinetic dissolution of Fe-Mn-carbonates and reproduction of trends for Fe^{2+} and Mn^{2+}

In Zuurbier et al., 2016, X-ray fluorescence (XRF) results indicated that carbonates in the deeper intervals of the aquifer were enriched with both Fe^{2+} and Mn^{2+} (Figure 3). With the kinetic dissolution of $FeCO_3$ and $MnCO_3$ added to the reaction network, the model was able to reproduce the trends observed at the ASR-wells for both Fe^{2+} and Mn^{2+} (Figure 16). While the relative trends for the both species were realized, simulated Fe^{2+} concentrations at AWS1 and AWS4 were higher than the observed Fe^{2+} concentrations during recovery in Cycles 1 and 2. However, the model simulated Mn^{2+} concentrations that matched the trends and concentrations of the observed data during recovery of both Cycles at the ASR-wells. During Cycles 5 and 6, simulations matched the observed concentrations for both Fe^{2+} and Mn^{2+} at AWS1.

At MW1S1, simulated Fe^{2+} concentrations matched the concentrations of the observed Fe^{2+} during all cycles, while the simulated Mn^{2+} concentrations were well above (~15 µM) the observed concentrations in Cycles 5 and 6. Similar trends were observed in MW1S2, where simulated Mn^{2+} concentrations were increased with respect to the observed concentrations.

3.2.4.3 Injection water impacts on Fe^{2+} and Mn^{2+}

Equilibrating the injection water with 5 mM of calcite showed that concentrations at AWS1 for both Fe^{2+} and Mn^{2+} were slightly decreased during Cycles 1 and 2 during recovery (Figure 16). During Cycle 8, Mn^{2+} concentrations were also decreased during the injection phase when compared to the base simulation. At AWS2, there was no change in concentrations for both species with injection water equilibrated with calcite. Increasing the O_2 concentration in the injection water showed that Mn^{2+} concentrations increased during Cycles 1 and 2 at AWS1, but Fe^{2+} concentrations were decreased.

3.2.4.4 Decommissioning effects on $Fe^{2+}$and Mn^{2+}

Decommissioning of the ASR-wells in Cycles 7 and 8 demonstrated that Mn^{2+} concentrations remained at 0 M until the end of Cycle 8, where only a slight increase to ~1 µM was observed at AWS1 (Figure 16). At AWS2, a much larger increase was observed, where concentrations reached nearly 50 µM by the end of Cycle 8. Fe^{2+} concentrations were unaffected at AWS1, where its concentration remained at 0 M, but a large increase was observed at AWS2 at the end of Cycle 8 (Figure 16).

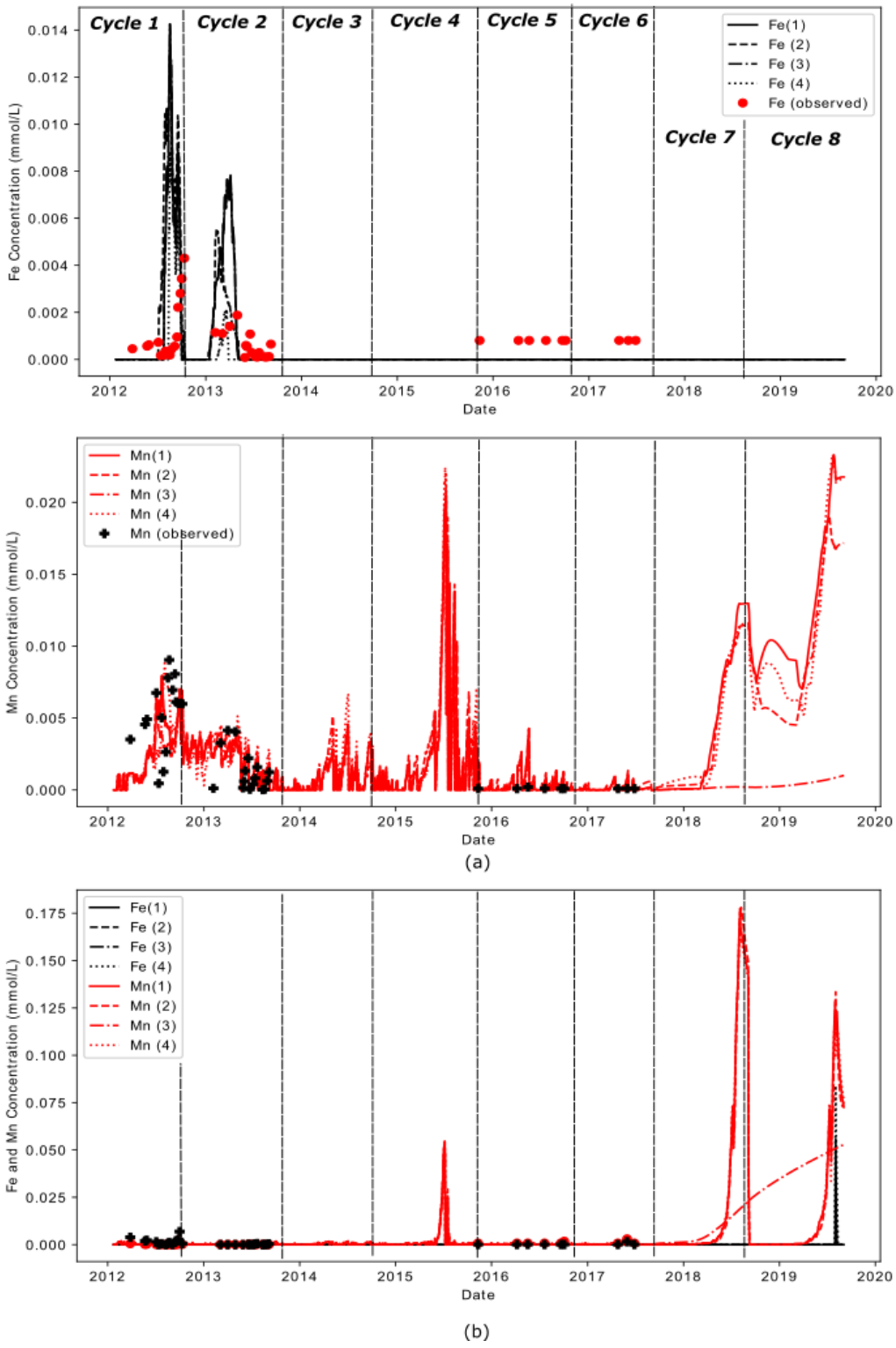

Figure 16: (a) The $Fe^{2+}$and Mn^{2+}concentrations at AWS1 and (b) the $Fe^{2+}$and Mn^{2+}concentrations at AWS2 for the different scenarios 1-4, listed in section 2.4.3, plotted with the observed concentrations for Fe^{2+} (red dots) and Mn^{2+} (black pluses). The figures for $Fe^{2+}$and Mn^{2} in (a) were split up in order to see the dynamic changes occurring in the initial cycles of ASR.

4. Discussion

4.1 MPPW-ASR and Reactive Impacts on the Injected Freshwater

MPPW-ASR was designed to increase the recovery of stored, relatively unmixed freshwater. At the Nootdorp ASR site, freshwater is injected into an anoxic, brackish aquifer during times of excess rain so that it may be stored for later irrigation use. Injection of a dissimilar water-type can lead to a myriad of reactions than can potentially alter the composition of the injected freshwater and subsequently deteriorate the water quality. Because the water quality limits for particular species set at this site are strict, being able to describe the major processes that affect the water quality is of great importance.

4.1.1 Dominance of Cation-Exchange in a Coastal Aquifer

Observations and reactive transport modeling demonstrated that during the first cycles of MPPW-ASR, the arrival of Na^+ at the primary recovery wells had a negative effect on the RE due to cation-exchange with Ca^{2+} in the injection water (Figure 7). An overall water-quality improvement in the upper three ASR-wells was observed in Cycles 5 and 6, where Na^+ concentrations in recovered water were below the desired limit. After multiple pore flushes, the Ca^{2+}-rich injection water clears the exchanger positions of Na^+ and other cations (mainly Fe^{2+}, Mn^{2+}, and NH_4^+) in the upper interval of the aquifer, which has been observed at similar sites [Stuyfzand, 1998].

Constant salinization (Na, Fe, and Mn adsorption: Table 4) of the deeper aquifer interval by the encroaching brackish water still threatens the success of the ASR-system. The ambient water rich in Na^+, Fe^{2+}, and Mn^{2+} moves under the freshwater bubble during times of recovery and allows for these cations to take up the exchanger positions. While MPPW-ASR injects in the bottom of the aquifer, this can potentially mobilize unwanted Na^+, Fe^{2+}, and Mn^{2+} during stages of injection, putting the injection water quality at risk. Reactive transport modeling showed that with a simple pumping and injection scheme, the mobilization of Na^+ through freshening (Table 4) directly affected the bulk recovered water, where during times of recovery in Cycles 7 and 8 were met with Na^+ concentrations exceeding the desired limit of 0.5 mM. This implies that a more dynamic pumping and injection scheme, where lengths of injection and recovery are shorter, is favorable for increasing the RE.

4.1.2 Redox Processes in a Coastal Aquifer

4.1.2.1 MPPW-ASR and ongoing pyrite oxidation

At the Nootdorp site, pyrite is a prevalent mineral throughout the length of the aquifer. Because Nootdorp uses surplus rain water, that is O_2-rich, for injection, pyrite oxidation is a dominant process that directly impacts the quality of the injection water. While pyrite oxidation releases SO_4^{2-} into the freshwater based on the reaction seen in table 4, the formation of $Fe(OH)_3$ and acidification of the injection water also occurs through proton-production. Through the geochemical analysis, the acidification of the lower aquifer interval by pyrite oxidation was suspected to be driving the dissolution of other minerals, mainly carbonates (Figure 9), at Nootdorp.

Reactive transport modeling demonstrated that upon injection during Cycle 1, pyrite oxidation in the deeper aquifer drove the dissolution of the Fe-Mn-Ca-carbonates, and subsequently created an undesirable Fe^{2+}-enriched zone near the bottom of the well. The enriched zone of Fe^{2+} is then able to consume O_2, forming $Fe(OH)_3$ (Table 4). This could explain why the extent of pyrite oxidation was calculated to be lower during Cycle 1 than in Cycle 2 at MW1S3 and MW1S4 (Table 7), where the O_2 is also consumed by dissolved and adsorbed Fe^{2+} and Mn^{2+} in the bottom of the well. It also explains why

the modeled SO_4^{2-} concentrations were elevated with respect to the observed concentrations at MW1S3 when Fe-Mn-carbonates were not included in the simulation (Figure 15) MPPW-ASR uses an injection scheme that preferentially injects water into the deeper intervals of the aquifer, which at the Nootdorp site is geochemically unfavorable. When applying MPPW-ASR, the order of reactive units that are located within an aquifer should be accounted for in order to optimize the RE of the system, especially when the standards for the site are strict.

Pyrite oxidation has been an ongoing process throughout the ASR-pilot. Modeling showed that even after two more ASR cycles, pyrite oxidation continues to acidify the injected freshwater. In the deeper intervals of the aquifer, it was seen that pyrite oxidation had consumed all the calcite available at AWS4 by the injection phase in Cycle 6. This means that no buffer for proton production is available at this well. The water will continue to acidify and potentially instigate other processes during transport to the recovery well. While the acidifying reactions cause dissolution of other minerals located throughout the aquifer matrix, this acidification can also lead to the release of Fe^{2+} or Mn^{2+} potentially bound to the formed $Fe(OH)_3$ by sorption processes [Appelo and Postma, 2005].

The release of trace metals into the injected water (specifically Zn^{2+} and As) via pyrite oxidation was suspected to be occurring at Nootdorp (Figure 12). It is likely that As is released upon pyrite oxidation into the injection water and, depending on the standards that are set for As, could negatively affect the RE [Smedley and Kinniburgh, 2002]. Contrarily, the acidification of the aquifer by pyrite would potentially promote sorption of As onto $Fe(OH)_3$ by giving the mineral surfaces a more positive charge and in turn, attracting anions (such as As, PO_4^{3-}, and HCO_3^-) through ionic forces [Appelo and Postma, 2005]. This type of process could explain why observed As concentrations are lowest in the lower aquifer interval, where more $Fe(OH)_3$ has formed and the pH remains lower due to the myriad of acidifying reactions. It could also explain why the observed As concentrations do not plot directly on the sediment ratio lines that are in Figure 12. It should also be noted that sorption of As onto $Fe(OH)_3$ could pose a threat near the lower intervals of the aquifer during recovery and upon decommissioning, where anoxic ambient water could potentially reduce the $Fe(OH)_3$, simultaneously mobilizing Fe^{2+} and As [Lazareva et al., 2015]. While pyrite is suspected to be source for As mobilization, it is unlikely that the Zn^{2+} observed are due to pyrite oxidation. Possibly, the observed Zn^{2+} concentrations are due to the Zn^{2+} that was found in the injection water and through mixing with the ambient water.

4.1.2.2 Mobilization and oxidation of Fe^{2+} and Mn^{2+}

The arrival of Fe^{2+} and Mn^{2+} to the recovery wells proved to be a risk for MPPW-ASR during the initial cycles at Nootdorp. The release of both Fe^{2+} and Mn^{2+} into the injection water was due to the dissolution of Fe-Mn-carbonates located at the bottom of the well upon proton-production by pyrite oxidation (Table 3). Reactive transport modeling demonstrated that the mobilized Mn^{2+} concentrations by $MnCO_3$ could not fully explain the observed Mn^{2+} concentrations, which were elevated with respect to Fe^{2+} (Figure 8). During the initial cycles of MPPW-ASR, a front of Fe^{2+}-rich water is formed through $FeCO_3$ dissolution at the bottom of the well. Because MPPW-ASR takes advantage of buoyancy effects, the Fe^{2+}-enriched front is transported to the top of the well, and with little $Fe(OH)_3$ or MnO_2 having formed in the shallower aquifer to provide sorption sites, Fe^{2+} can deteriorate the quality of the recovered water.

The reduction of MnO_2 by Fe^{2+} (Table 3) was suspected to be the dominant process that mobilizes the highly unwanted Mn^{2+} concentrations and severely deteriorates the water quality (Figure 8). While

modeling shows that MnO_2 was forming near the top of the well during the initial stages of MPPW-ASR, the mobilized Fe^{2+}-front that is transported from the bottom of the well reduces the mineral during recovery. This explains why an elevated Mn:Fe ratio is observed during the recovery stages of Cycle 1, which contradicts the more Fe^{2+}-rich ambient water (469 µM for Fe^{2+} and 19 µM of Mn^{2+}). In later cycles, the arrival of Mn^{2+} and Fe^{2+} at the recovery wells is less prevalent. Modeling showed that by the end of Cycle 1, all the Fe-carbonates located near the ASR-wells had been completely dissolved, but some Mn-carbonates did not completely dissolve near the top of the ASR-well until the end of Cycle 3. This result can also explain why the calculated extent of pyrite oxidation increased from Cycle 1 to Cycle 2 for MW1S3 and MW1S4 (Table 7). Without the release of Fe^{2+} through Fe-carbonate dissolution, more O_2 can be consumed by the pyrite that is available at these wells.

The lack of Fe- carbonates in combination with the adjusted pumping/injection scheme for SIR (Cycle 2: Table 5) was able to oxidize the mobilized Fe^{2+} and Mn^{2+} and form $Fe(OH)_3$ and MnO_2 near the recovery wells. The formation of these minerals creates more sorption sites that can potentially adsorb Fe^{2+} and Mn^{2+} that travel to the recovery wells. This could explain why in subsequent cycles (Cycles 5 and 6), undetectable concentrations for Fe^{2+} and Mn^{2+} were observed near the primary recovery wells (Figure 8). While virtually no Fe^{2+} and Mn^{2+} was found in the recovered water during Cycles 5 and 6, the water quality is still at risk due to the encroaching brackish water transporting ambient Mn^{2+} to the bottom ASR-wells during recovery. This in turn leads to a persistent formation of MnO_2 during stages of injection, and reduction by Fe^{2+} occurring in the bottom of the well during stages of recovery.

The injection water composition, ambient water composition, initial aquifer matrix composition, and standards set for the site could either have a net negative or net positive effect on the RE with respect to Fe^{2+} and Mn^{2+}. Increasing O_2 concentrations in the injection water allowed pyrite to dissolve the Fe-Mn-carbonates at a quicker rate, and in turn created a more Mn^{2+}-rich water at the recovery wells than observed in Cycles 1 and 2 (Figure 16). However, during Cycles 5 and 6, increasing the O_2 concentration was able to produce lower Mn^{2+} and Fe^{2+} concentrations at the recovery wells due to increased oxidation of both species. This same trend was observed in the simulated Cycles 7 and 8 (Figure 16). Simulations where the injection water was equilibrated with 5 mmol/L of calcite were able to produce lower Fe^{2+} and Mn^{2+} concentrations, but recovered water still contained concentrations that were too high for the Nootdorp standards in the initial cycles (Figure 16).

4.1.3 Overall Assessment of the Impact of MPPW-ASR on the Injection Water

MPPW-ASR has the ability to increase the RE of injected freshwater in a coastal aquifer with respect to conservative Cl^- concentrations [Zuurbier et al., 2014]. However, reactive transport processes during MPPW-ASR caused by interactions between the aquifer matrix and the injection water can severely deteriorate the injection water quality. With observational data and reactive transport modeling, the long-term impact that MPPW-ASR has on the injection water is overall a positive outcome. Observational data from Cycles 5 and 6 indicated that concentrations for Na^+, Fe^{2+}, and Mn^{2+} were at acceptable levels in the recovered water throughout both cycles. Processes like cation-exchange and Fe-Mn-carbonate dissolution that were major factors in determining the composition of the recovered water during Cycles 1 and 2 were not as prevalent in Cycles 5 and 6. The oxidation of Fe^{2+} and Mn^{2+}, pyrite oxidation, trace metal sorption, and the reduction of MnO_2 by Fe^{2+} are the more dominant reactions that are occurring during these later cycles.

The injection of freshwater into the lower intervals of the Nootdorp aquifer during MPPW-ASR has a profound impact on the quality of water. These intervals are pyrite-rich, as well as contain Fe-Mn-carbonates, and the dissolution of these minerals can severely decrease the RE. The encroaching brackish water consistently brings unwanted Na^+, Fe^{2+}, and Mn^{2+} to AWS4 during recovery stages of MPPW-ASR. This implies that there is still a potential risk of recovering deteriorated water when injection into these highly reactive units is occurring.

4.2 MPPW-ASR Reactive Impact on Surrounding Brackish Water

Reactive transport processes can affect not only the injected freshwater, but also the surrounding brackish water through mixing at the fringe of the freshwater-saltwater interface. Through persistent injection into the aquifer, the ambient water that surrounds the freshwater bubble becomes diluted and will also exhibit buoyant flow through density-differences. This implies that the water formed near the bottom of the well will also be transported to near the top of the well and away from the ASR-wells.

Modeling showed the surrounding brackish water composition in the beginning Cycles 1 and 2 switched from a Na-Cl water-type to a more Na-HCO_3^- water-type in the deeper intervals. While the composition was similar to the initial concentrations observed, it is depleted with respect to Na^+ and enriched in HCO_3^-. This can be attributed to the dissolution of carbonates in the deeper aquifer near the ASR-wells increasing the composition of HCO_3^- in the water based on the reaction in table 4. Subsequent cycles though, showed the brackish water switch back to a Na-Cl water-type. Likely, this is because the Fe-Mn-carbonates become completely dissolved and cannot produce more HCO_3^- that can be transported away from the ASR-wells.

4.3 Model Limitations and Potential Modeling

4.3.1 Limitations and Remarks for Modeling Nootdorp

While the reactive transport model simulated the observed concentrations for multiple different species relatively well, there are still some uncertainties for the model. One in particular is the laterally heterogeneous nature that is present in the Nootdorp aquifer. While the reactive transport model assumed that the system was laterally homogenous in composition, this is not entirely true for the actual aquifer. Subtle differences in aquifer matrix composition, as well as ambient water composition, that may be observed laterally will affect the observed concentrations and may not be predicted by the model.

Some other uncertainties that can affect the output of the model are the constant injection composition and constant temperature throughout the model simulations. By having a constant injection composition, the model cannot predict the changes that occur in reality, where injection compositions, mainly O_2 and Ca^{2+}, varied throughout the ASR-pilot. This can affect the extent of redox processes, such as pyrite oxidation and oxidation of dissolved species, as well as potentially affect cation-exchange outputs. Having a constant temperature in the model means that the seasonal variability that can affect reactive processes, such as pyrite oxidation and calcite dissolution [Appelo and Postma, 2005], is not possible. The formation of $Fe(OH)_3$ and MnO_2 minerals that occur at Nootdorp could potentially affect the permeability of the aquifer, and this also cannot be predicted by the model.

Likely, the largest uncertainty that comes from the reactive transport model is the fact that the non-continuous clayey interval cannot be included in the model. This clay interval potentially affects the flow patterns in the observed aquifer greatly by forcing water into more permeable zones. This could overall

affect the composition of the water that is transported throughout the aquifer and could produce results that are not observed. This could help explain why concentrations for Mn^{2+} at MW1S1 and MW1S2 were predicted to be higher than the observed results show. While the clay interval would potentially prevent the dissolution of Fe-carbonates in the clay, as well as prevent the upconing of the Fe^{2+}-rich bottom water produced, the reduction of MnO_2 would not be able to occur to the extent that it did at these wells, ultimately leading to lower Mn^{2+} concentrations.

4.3.2 Further Modeling

While the inclusion of the multiple redox processes to the Nootdorp model can partially describe the geochemistry of the site, further modeling must be done to help improve the model output. Due to the observed As that is produced in the injection water, modeling the release of As by pyrite oxidation could be added to the model. Along with this, a surface complexation model to account for sorption of species onto $Fe(OH)_3$ could be added for a more accurate simulation. The increased Fe^{2+} ratios seen at AWS1 in figure 16 could potentially be due to the lack of a surface complexation model. The rate constants for the kinetic geochemical processes were taken from previous studies, but the data could possibly be fitted through parameter estimation to obtain more accurate rate constants specific to the Nootdorp site. Heterogenous reactions involving adsorbed Fe^{2+} and Mn^{2+} could also potentially contribute heavily to the model. With these processes included into the model, the complex nature of Fe^{2+} and Mn^{2+} may be better described, as they would contribute the decreasing trends for both species.

5. Conclusion

MPPW-ASR has demonstrated that in a coastal brackish aquifer, the RE of injected freshwater can be increased when applying this ASR-system. While MPPW-ASR was shown to increase the RE with respect to mixing effects and conservative Cl^- concentrations, reactive transport modeling combined with geochemical analysis highlights the complex geochemical nature of the Nootdorp site. With the inclusion of redox processes and the dissolution of Fe-Mn-carbonates to the Noordorp model, more of the complex geochemistry of this site could be described.

Injection of rainwater combined with the reduced conditions of this aquifer initiate an increase in Na^+, Fe^{2+}, and Mn^{2+} that deteriorate the quality of the injected water through pyrite oxidation, dissolution of Fe-Mn-carbonates, reductive dissolution of MnO_2, and cation-exchange in initial cycles. Over time through dilution, oxidation, and sorption, these species are able to show decreased concentrations at AWS1 and AWS2, but continuous salinization and reductive dissolution of Fe^{2+} and Mn^{2+} bearing minerals at the bottom of the aquifer continues to deteriorate the water quality. While the injection water composition is altered, the surrounding brackish water composition is also affected. Through density-dependent flow and mixing, an enrichment in HCO_3^- and depletion in Na^+ were observed in the surrounding brackish water.

When applying MPPW-ASR to other locations, an intensive geochemical analysis of the aquifer is required. Based on the geochemical composition that a coastal aquifer may have, as well as the injection water composition, different geochemical processes may occur. This will affect the overall injection water geochemistry and along with the standards that are set for a specific site, could affect the overall RE of the system. Therefore, careful consideration for the placement of ASR wells, as well as the injection scheme, should also be considered.

6. References

Andersen, M.S., Larsen, F., and Postma, D., 2001. Pyrite oxidation in unsaturated aquifer sediments. Reaction stoichiometry and rate of oxidation. Environ. Sci. Technol. 35, 4074-4079.

Antoniou, E.A., Stuygzand, P.J., and van Breukelen, B.M., 2013. Reactive transport modeling of an aquifer storage and recovery (ASR) pilor to assess long-term water quality improvements and potential solutions. Appl. Geochem. 35, 173-186.

Antoniou, E.A., van Breukelen, B.M., and Stuyfzand, P.J., 2015. Optimizing aquifer storage and recovery performance through reactive transport modeling. Appl. Geochem. 61 (0), 29-40.

Appelo, C.A.J. and Postma, D., 2005. Geochemistry, Groundwater and Pollution, 2. A.A. Balkem, Leiden, The Netherlands, p. 162.

Bakker, M., Post, V., Langevin, C.D., Hughes, J.D., White, J.T., Starn, J.J., and Fienen, M.N., 2016. Scripting MODFLOW Model Development Using Python and FloPy. Groundwater, p. 1-7.

Hartog, N., Griffioen, J., van der Weijden, C.H., 2002. Distribution and reactivity of O2-Reducing components in sediments from a layered aquifer. Environ. Sci. Technol. 36 (11), 2338-2344.

Herczeg, A.L., Rattray, K.J., Dillon, P.J., Pavelic, P., and Barry, K.E., 2005. Geochemical Processes During Five Years of Aquifer Storage Recovery. Groundwater 39 (5).

Izbicki, J.A., Petersen, C.E., Glotzbach, K.J., Metzger, L., Christensen, A.H., Smith, G.A., O'Leary, D., Fram, M.S., Joseph, T., and Shannon, H., 2010. Aquifer Storage Recovery (ASR) of chlorinated municipal drinking water in a confined aquifer. Appl. Geochem. 25 (8).

Langevin, C.D., Thorne, D.T., Dausman, A.M., Sukop, M.C., and Guo, W., 2007. SEAWAT version 4: a computer program for simulation of multi-species solute and heat transport. In: U.S.G.S. (Ed.), Techniques and Methods, Book 6, Reston, Virginia, USA.

Langevin, C.D., 2008. Modeling Axisymmetric Flow and Transport. Groundwater, 46 (4), p. 579-590.

Lazareva, O., Druschel, G., and Pichler, T., 2015. Understanding arsenic behavior in carbonate aquifers: implications for aquifer storage and recovery (ASR). Appl. Geochem. 52 (0), 57-66.

Lowry, C.S. and Anderson, M.P., 2006. An Assessment of Aquifer Storage Recovery Using Ground Water Flow Models. Groundwater, 44 (5), 661-667.

Missimer, T.M., Guo, W., and Walker, C.W., 2002. Hydraulic and density considerations in the design of aquifer storage and recovery systems. Florida Water Resources Journal 55 (2), 30-36.

Oude Essink, G.H.P., van Baaren, E.S., and de Louw, P.G.B., 2010. Effects of climate change on coastal groundwater systems: A modeling study in the Netherlands. Water Resour. Res., 46, 1-16.

Parkhurst, D.L., Appelo, C.A.J., 1999. User's Guide to PHREEQC (Version 2): a Computer Program for Speciation, Batch-reaction, One-dimensional Transport, and Inverse Geochemical Calculations. Water-resources Invesitgations Report; 99-4259. U.S. Geological Survey: Earth Science Information Center, Open-File Reports Section [distributor], Denver, Colorado, USA.

Postma, D. and Appelo, C.A.J, 2000. Reduction of Mn-oxides by ferrous iron in a flow system: Column experiment and reactive transport modeling. Geochim. Et Cosmoch. Acta 64 (7), 1237-1247.

Pyne, R.D.G., 2005. Aquifer Storage Recovery – a Guide to Groundwater Recharge through Wells. ASR Sysems LLC, Gainesville, Florida, USA.

Ros, S.E.M. and Zuurbier, K.G., 2017. The Impact of Integrated Aquifer Storage and Recovery and Brackish Water Reverse Osmosis (ASRRO) on a Coastal Groundwater System. Water, 9 (4), 273.

Smedley, P.L. and Kinniburgh, D.G., 2002. A review of the source, behaviour and distribution of arsenic in natural waters. Appl. Geochem. 17, 517-568.

Stuyfzand, P.J., 1998. Quality changes upon injection into anoxic aquifers in the Netherlands: evaluation of 11 experiments. In: Peter, J.H. (Ed.), Artificial Recharge. Balkema, Amsterdam, The Netherlands, pp. 283-291.

TNO, 1995. Interpolated Isohypses (28-4-1995). In: TNO (Ed.), Utrecht, The Netherlands

Wallis, I., Prommer, H., Post, V., Vandenbohede, A., and Simmons, C.T., 2013. Simulating MODFLOW-Based Reactive Transport Under Radially Symmetric Flow Conditions. Groundwater, 51 (3), p. 398-413.

Ward, J.D., Simmons, C.T., and Dillon, P.J., 2008. Variable-density modelling of multiple-cycle aquifer storage and recovery (ASR): Importance of anisotropy and layered heterogeneity in brackish aquifers. J. Hydrol., 356, 93-105.

Ward, J.D., Simmons, C.T., Dillon, P.J., and Pavelic, P., 2009. Integrated assessment of lateral flow, density effects and dispersion in aquifer storage and recovery. J. Hydrol., 370, 83-99.

Williamson, M.A. and Rimstidt, J.D., 1994. The kinetics and electrochemical rate-determining step of aqueous pyrite oxidation. Geochim. et Cosmochim. Acta, 58 (24), 5443-5454.

Zuurbier, K.G., Zaadnoordijk, W.J., and Stuyfzand, P., 2014. How multiple partially penetrating wells improe the freshwater recovery of coastal aquifer storage and recovery (ASR) systems: a field and modeling study. J. Hydrol. 509, 430-441.

Zuurbier, K.G., 2016. Increasing freshwater recovery upon aquifer storage: A field and modelling study of dedicated aquifer storage and recovery configurations in brackish-saline aquifers (Doctoral dissertation). Retrieved from https://repository.tudelft.nl/islandora/object/uuid:4631f3d2-14ff-4505-bcba-0c21956c460f?collection=research. doi:10.4233/uuid:4631f3d2-14ff-4505-bcba-0c21956c460f.

Zuurbier, K.G., Hartog, N., and Stuyfzand, P.J., 2016. Reactive transport impacts on recovered freshwater quality during multiple partially penetrating wells (MPPW-)ASR in a brackish heterogeneous aquifer. Appl. Geochem. 71, 35-47.

Zuurbier, K.G., van Dooren, T., and Ros, S., 2017. Improved ASR-Coastal Reference sites in Nootdorp and Westland, the Netherlands (TRL8). Retrieved from KWR Watercycle Research Institute.